Accepted Manuscript

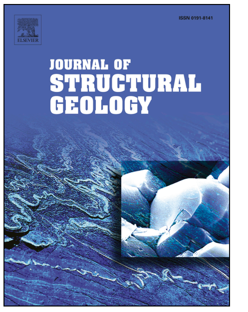

Fault deformation, seismic amplitude and unsupervised fault facies analysis: Snøhvit Field, Barents Sea

Jennifer Cunningham, Nestor Cardozo, Christopher Townsend, David Iacopini, Gard Ole Wærum

PII: S0191-8141(18)30328-6

DOI: 10.1016/j.jsg.2018.10.010

Reference: SG 3761

To appear in: *Journal of Structural Geology*

Received Date: 10 June 2018

Revised Date: 11 October 2018

Accepted Date: 11 October 2018

Please cite this article as: Cunningham, J., Cardozo, N., Townsend, C., Iacopini, D., Wærum, G.O., Fault deformation, seismic amplitude and unsupervised fault facies analysis: Snøhvit Field, Barents Sea, *Journal of Structural Geology* (2018), doi: https://doi.org/10.1016/j.jsg.2018.10.010.

Fault deformation, seismic amplitude and unsupervised fault facies analysis: Snøhvit field, Barents Sea

*Jennifer CUNNINGHAM * [A], Nestor CARDOZO [A], Christopher TOWNSEND [A], David IACOPINI [B] and Gard Ole WÆRUM [C]*

[A] *Department of Energy Resources, University of Stavanger, 4036 Stavanger, Norway*

**jennifer.e.cunningham@uis.no , +47 461 84 478*

nestor.cardozo@uis.no , chris.townsend@uis.no

[B] *Geology and Petroleum Geology, School of Geosciences, University of Aberdeen, Meston Building, AB24 FX, UK*

d.iacopini@abdn.ac.uk

[C] *Equinor ASA, Margrete Jørgensens Veg 4, 9406 Harstad, Norway*

gawa@equinor.com

Keywords: faults, dip distortion, seismic attributes, seismic amplitude, fault facies.

Abstract

We present an integrated seismic imaging and fault interpretation workflow to characterize the seismic expression in and around an E-W trending central fault system imaged in near-angle stack seismic data of the Snøhvit Field, Barents Sea. Three E-W normal fault systems offset five Triassic-Lower Cretaceous seismic horizons across the field. Fault throw is largest at depth and decreases with shallowing. Dip distortion (DD) decreases in magnitude and extent with shallowing. Fault enhancement (FE), a filter used to detect edges, was applied on a blend of tensor, semblance and dip attributes, and allowed us to classify fault zones into four unsupervised seismic fault facies (mid-high FE). High FE facies occur at the center of the fault zones and are abundant in the highest thrown eastern part of the field. The FE facies decrease radially outwards field wide. Facies correlate with throw and dip separation gradient, which are in turn related to mechanical stratigraphy controlling fault propagation. We observe systematic seismic amplitude variations: a major amplitude drop on the fault plane, and a brightening and dimming linked to fault-related synclines and anticlines, respectively. Our workflow establishes a methodology for fault interpretation, linking fault throw, DD, seismic attributes and fault facies classification.

1. Introduction

Outcrop studies provide a large amount of information pertaining to fault displacement, structure, and the chemical and physical processes involved in the formation and growth of faults on both large and small scales (e.g. Barnett et al., 1987; Childs et al., 1995, 2009; Eichhubl et al., 2005). However, in a subsurface environment, seismic and well data don't always give the necessary information about faults, and outcrop data are far more difficult to extrapolate to the subsurface (i.e. Townsend et al., 1998; Aarland and Skjerven, 1998; Færseth et al., 2007; Dutzer et al., 2010; Iacopini et al., 2016). In the rare chance that a well intersects a fault and core is collected from the well, vast amounts of geological and petrophysical information are collected from a small rock volume contained in the fault (Aarland and Skjerven, 1998; Færseth et al., 2007). These core data then need extrapolation across the field using seismic data. Since a well crosscutting a fault is a rarity, seismic data remain the most used method of investigation of faults in the subsurface (e.g. Townsend et al., 1998; Dutzer et al., 2010; Iacopini et al., 2016). In comparison to well data, seismic data provide a broader 3D understanding of faults, their displacement, linkages, and facies changes both vertically and laterally. Seismic resolution, however, often presents a problem when interpreting subsurface faults (Gauthier and Lake, 1993; Townsend et al., 1998; Dutzer et al., 2010; Long and Imber, 2011). For typical exploration conditions (wavelet frequency = 30 Hz, velocity = 3000 m/s), the vertical resolution is about 25 m (¼ of the wavelength or tuning thickness), and the lateral resolution after data migration is about 50 m (½ of the wavelength or effective Fresnel zone diameter; Ashcroft, 2011). However, in the vertical a bed will still be detectable well below tuning thickness (Widess, 1973).

Another common issue in reflection seismology when imaging faults is diffraction, which occurs when a seismic wave interacts with a discontinuity (fault) or lateral heterogeneity, generating a radially scattered diffracted wave (Landa and Keymar, 1998; Townsend et al., 1998). Seismic data, however, are standardly processed for reflections (lithological boundaries) rather than diffractions (faults), which are removed during data migration (Landa, 2007, 2012).

A number of studies have aimed to characterize in detail faults in seismic data. Townsend et al. (1998) was the first comprehensive analysis of small-scale faults using amplitude anomalies in seismic reflection data. Dutzer et al. (2010) used seismic attribute analysis to study fault architecture and sealing potential. Long and Imber (2010, 2012) introduced new techniques in seismic reflector dip sampling to generate maps of fault related deformation (dip distortion) in a normal fault array and a relay zone. These methods focused more on extracting deformation patterns from the interpreted data, rather than attributes applied specifically to the seismic data. Iacopini and Butler (2011) and Iacopini et al. (2012) designed a visualization workflow combining seismic attributes, opacity filtering and spectral decomposition to characterize deformation surrounding thrusts in deep marine settings. Iacopini et al. (2016) used crossplots of tensor, semblance and instantaneous phase attributes to resolve the seismic expression of normal fault damage. They also introduced the term seismic disturbance zones (complex volumes of disrupted seismic signal around faults; SDZ) and proposed methods to map unsupervised seismic fault facies within these zones (Iacopini et al., 2016). These facies are reconstructed through simple statistical cross plotting approaches but are not directly linked to actual geological data, such as log data or core samples (Dumay and Fournier, 1988; Posamentier and Kolla, 2003; Iacopini et al., 2016).

An alternative approach to investigate and understand the significance of seismic geobodies is through the use of forward seismic modelling (Carcione et al., 2002 and sources therein). Synthetic seismic modelling has been applied to simulate the seismic expression of faults and has uncovered a wealth of knowledge with respect to the seismic imaging of fault zones (e.g. Botter et al., 2014, 2016, 2017a-b). These studies concluded that there is a direct correlation between amplitude changes across the fault and fault-related deformation, thus confirming the plausibility of exploring fault zones through the use of seismic attributes (e.g. Botter et al., 2014, 2016).

The purpose of this work is to explore existing and new techniques in fault analysis to investigate the geological significance of seismic geobodies enveloping faults. We also test on real seismic data some of the findings from seismic modelling by Botter et al. (2014, 2016, 2017a-b). To accomplish these objectives, we use pre-stack depth migrated, near-angle stack and depth converted 3D seismic data from the Snøhvit Field, southwest Barents Sea, Norway. Our study focuses on fault-related deformation of the Upper Triassic-Lower Cretaceous interval (1.5-3 km depth) using a methodology that includes data conditioning, structure maps, fault throw, dip distortion, seismic attributes, seismic fault facies, and seismic amplitudes. The seismically interpreted fault structure lacks well control, but it correlates with structural parameters such as fault juxtaposition and dip separation gradient (strain). Thus, the proposed methodology has the potential for realistic unsupervised characterization of faults in the subsurface.

2. Geological setting

The Snøhvit Field is located in the Norwegian southwest Barents Sea in the center of the Hammerfest Basin (Fig. 1 a, b; Linjordet and Olsen, 1992). The Hammerfest Basin is a downthrown ENE-WSW rift basin, which began to develop during the Late Jurassic- Early Cretaceous (Fig. 1a; Sund et al., 1984; Berglund et al., 1986; Linjordet and Olsen, 1992; Ostanin et al., 2012). The basin is 150 km long by 70 km wide and is bound to the north by the Loppa High, along the southeast margin by the Finnmark Platform and to the west by the Tromsø Basin (Sund et al., 1984; Doré, 1995; Ostanin et al., 2012). The main subsidence of the Hammerfest Basin was controlled by NE-SW basin bounding faults in the Early Cretaceous (Fig. 1 a; Sund et al., 1984; Linjordet and Olsen, 1992). These faults are responsible for the preservation of Triassic and Jurassic sediments, and the subsequent deposition of the Cretaceous and Tertiary sediments (Berglund et al., 1986). The basin deepens and widens westward and therefore the Triassic-Cretaceous succession is thicker in the west than in the east (Linjordet and Olsen, 1992). Upper Triassic-Lower Cretaceous pre- and syn- rift strata are the focus of this paper. An E-W trending central fault system that lies between the main basin bounding faults was formed during basin extension due to the presence of a dome parallel to the Hammerfest Basin axis (Sund et al., 1984). Some of these faults are the focus of this study (Fig. 1 a, b; Linjordet and Olsen, 1992). **INSERT FIGURE 1**

The Snøhvit gas field was discovered in 1984 and at the time it was the largest gas find in the Barents Sea (Linjordet and Olsen, 1992). The generation, migration and distribution of hydrocarbons in the Snøhvit Field is controlled by the E-W trending fault system which segments the hydrocarbon plays into northern and southern provinces (Sund et al., 1984). The organic rich shales of the Triassic Kobbe and Snadd Fms and the Jurassic Hekkingen Fm are the main source rocks in the area (Linjordet and Olsen, 1992). The reservoir intervals are the Lower-Middle Jurassic sandstones of the Tubåen, Nordmela and Stø Fms (Linjordet and Olsen, 1992). The Jurassic Fuglen and Hekkingen Fms are the main sealing intervals (Linjordet and Olsen, 1992).

Five Upper Triassic-Early Cretaceous seismic horizons were chosen for interpretation as they give the most representative assessment of faulting throughout the studied interval (Fig. 1c, d; interpreted horizons E to A). The deepest Upper Triassic - Lower Jurassic Fruholmen Fm consists of open marine shales interbedded with fluviodeltaic sandstones and coals (Dalland et al., 1988). The Middle-Upper Jurassic Fuglen Fm is present across the entire basin and consists of mudstones interbedded with limestones, which were deposited during a sea-level highstand in a fully marine environment (Dalland et al., 1988; Linjordet and Olsen, 1992). The Lower Cretaceous Knurr Fm (deposited in an open, distal marine environment) is a claystone containing interbeds of thin limestones and dolomites, as well as sandy intervals towards the base (Dalland et al., 1988). The Lower Cretaceous Kolje Fm (deposited in an open, distal marine environment) is a shale and claystone unit containing some minor interbeds of limestone, dolomite, siltstone and sandstone towards the top (Dalland et al., 1988).

3. Methodology

We integrate seismic interpretation, image processing and fault analysis methods into a single workflow (Fig. 2) that is designed to uncover information about the 3D geometry and internal structure of faults. The workflow integrates new and existent methods (Fig. 2). The newly introduced method is the analysis of seismic amplitude versus distance to fault. The data conditioning, seismic interpretation, fault throw analysis, dip distortion, and the use of seismic attributes are previously used methods that are combined in this study (Rippon, 1985; Long and Imber, 2010, 2012, Iacopini et al., 2012, 2016; Gilani and Gómez-Martínez, 2013; Wilson et al., 2013; Botter et al., 2017a). The computer programs Geoteric, OpendTect, Petrel and TrapTester (T7) were used to execute the workflow. 3D Seismic survey ST15M04, a merge of five 3D seismic surveys (produced by Equinor ASA and their partners) is the main dataset of the study. The area of interest, chosen directly above the Snøhvit Field, from within the ST15M04 volume, covers ~25 km in the E-W direction and ~5 km in the N-S direction, and has inline and crossline spacing of 12.5 m (orange rectangle, Fig. 1b). The data have been pre-stack depth migrated (Kirchhoff), zero phased, stacks were generated (full and partial), and finally the data were converted to the depth domain where it is assumed the velocity model is correct and the vertical scale of the data is depth. In this dataset an increase of impedance is represented by a red peak (blue-red-blue). All steps in the workflow were conducted on the near-angle (5-20°) stack since this volume maintains the most consistent reflector continuity and the best structural detail, as proved by studies of reflection coefficient versus incident angle (Shuey, 1985 and references therein). It is not possible to ascertain the shooting direction of this volume because, as mentioned, the data used are a merge of multiple datasets and vintages. **INSERT FIGURE 2**

3.1 Data conditioning

In the area of interest, seismic data quality is generally excellent. However, shallow gas in the west and north, and a thick dolomite unit in the east significantly decreases the signal-noise ratio at the depth range of interpretation (1.5-3 km). To counter this problem, a noise attenuation and amplitude normalization workflow was applied (Fig. 3). There are two types of noise. First, an aggressive type of noise caused by gas and dolomites, and second, a minor coherent and random noise. To target these noise variations, two field-wide seismic volumes were generated using passive and aggressive noise attenuation (Fig. 3), following a procedure that involved two steps of noise cancelation, and filters described in detail by Gilani and Gómez-Martínez (2013). The resultant volumes were merged using a chaos attribute mask volume (masked values: 6270-17000) that applies aggressive noise cancelation to areas with low signal-noise ratio and passive noise attenuation everywhere else (Fig. 3; Gilani and Gómez-Martínez, 2013). In areas of low amplitude (identified by the chaos mask volume), a scaling factor (1.75) was applied to normalize the seismic signal (Fig. 3; Gilani and Gómez-Martínez, 2013). During the application of data conditioning, it was important not only to remove noise, but also to maintain the signal that was already present in the data. The noise removed was monitored in each stage of the workflow to ensure only random noise was removed, and the signal associated with seismic reflectors and faults were unaltered.

INSERT FIGURE 3

3.2 Seismic interpretation using near-angle stack

The interpretations were completed on the near-angle stack (5-20°) volume that was created after data conditioning. The selected horizon tops are bright, laterally extensive reflectors, which can be interpreted across the entire field and main faulted interval. The horizon tops are picked on mostly peaks (top Fruholmen, top Fuglen, top Knurr and top Kolje) and a single trough (intra-Kolje). Faults were interpreted using a dense interpretation grid of 16 inlines, while horizons were auto-tracked between faults (Yielding and Freeman, 2016). The interpretations were quality controlled by studying the intersections between horizons and faults (fault cutoffs) and throw distribution on faults (next section).

3.3 Fault throw analysis

Fault throw is the vertical component of the dip separation, which is the vector connecting the hanging wall and footwall cutoffs along the fault dip direction (Fig 4a). When constraining the fault cutoffs, user-defined trim and patch distances were used to account for interpretation errors near the fault (Fig. 4; Wilson et al., 2009, 2013; Elliott et al., 2012). ‘Trim’ is a distance applied to both sides of the interpreted fault plane that is designed to omit data too near the fault plane that may skew the overall throw results (Fig 4b; Wilson et al., 2009). The ‘patch’ is the distance immediately beyond the trim, which defines a volume of high horizon interpretation confidence that can be projected onto the interpreted fault plane to create the cutoffs (Fig. 4b; Wilson et al., 2009, 2013; Yielding and Freeman, 2016). Trim and patch distances of 50 and 75 m respectively were chosen after thorough testing, in order to produce the cutoffs that deliver the most representative displacement patterns for each horizon of interest. Anomalies in the throw distributions were used as a quality control process to identify inconsistencies in interpretation. These anomalies were fixed by editing fault and horizon interpretations where necessary. **INSERT FIGURE 4**

3.4 Dip distortion

The term dip distortion (or apparent dip, DD) is used to describe the volume of deformation surrounding the faults, from which horizons depart from their regional dip (Long and Imber, 2010, 2012). The main input for calculating DD are the interpreted horizons, which were used to generate high-resolution triangulated surfaces (trimeshes). These trimeshes were sampled along N-S transect lines which are oriented approximately perpendicular to the E-W trending faults with the largest throw. Along each transect, there are points which coincide to corner points on the trimesh horizon (Fig. 4c, points A, B). Between each of these points a measurement of the distance (x) and the differential depth (z) between the points is taken. From these two values, θ or apparent dip (DD) is computed (Fig. 4c). The computed DD values are then reimported as point sets and used as the main input to create maps (Fig. 4c). These DD maps show the apparent dip projected onto a horizontal plane at the average horizon depth.

3.5 Seismic attribute analysis

Seismic attribute analysis was conducted to improve the imaging of faults and isolate seismic fault signatures. The near-angle stack, data conditioned seismic volume was used as the input for generating tensor, semblance, dip and envelope attribute volumes. These attributes were chosen as they were the three most successful attributes in fault detection for this study. The tensor attribute is based on a structurally-oriented symmetric tensor whose principal axes define the local reflector orientation (Bakker, 2002). This attribute is sensitive to changes in amplitude and reflector continuity and is suited to imaging large scale faults where seismic expression may differ laterally (Bakker, 2002). The semblance attribute identifies reflector discontinuity and distortions within the data volume (Marfurt et al., 1998). The dip attribute is defined as a measure of reflector inclination with respect to the horizontal (Barnes, 2000; Marfurt, 2006). The dip attribute can be used to calculate the orientation and magnitude of structural and/or stratigraphic edges within a seismic volume, for example faults or lateral lithological changes (Purves and Basford, 2011; Alaei, 2016). It is important to note that the dip attribute is a measurement of changes to the seismic reflector while the DD in section 3.4 is a measure of the apparent dip of the interpreted seismic horizons. Envelope is also known as instantaneous amplitude and is a measure of reflection strength (Taner et al., 1979). The tensor and semblance attributes were run using a fault width of 7 and a height of 21 voxels while the dip had a fault width of 5 and a height of 21 voxels (these settings were optimized for faults > 60 m long). An equally weighted CMY (Cyan, Magenta and Yellow) color blend of two coherence attributes (tensor and semblance) and a dip attribute provided a more complete understanding of the fault bodies. When high values of tensor, semblance and dip occur simultaneously, the color displayed is black. Since the blended attributes in this case are structure or edge enhancing, the dark colors in the CMY volume are associated to faults.

3.6 Fault enhancement and seismic fault facies

The fault enhancement (FE) filter is a Gaussian filter that is applied to enhance the edges in a seismic volume while also suppressing noise (Chopra and Marfurt, 2007). In this case the FE filter is applied to a greyscale conversion of the tensor, semblance and dip CMY color blend, where the highest color saturations in the color blend are represented as the darkest greys in the greyscale volume. The application of the FE filter is defined using a three-dimensional matrix of sigma values corresponding to the standard deviation of the Gaussian filter. In this study, a matrix of weight factors of 3 (x direction), 3 (y direction) and 6 (z direction) were assigned to generate the FE volume. These factors represent the contribution of a voxel at a given location to the FE attribute in the center of the filter, where a factor of 3 or 6 means that 68% of the energy of the filter is localized within ± 3 or 6 voxels around the central voxel, respectively. After applying the FE filter, noise contained in the color blend volume of attributes is attenuated and dispersed across many voxels while the intensity of the discontinuity remains (Chopra and Marfurt, 2007). The greyscale volume was limited in depth to 2110-2750 m (to only include the top Fuglen and top Knurr) where the imaging of faults is the clearest and the least amount of noise is present. The dynamic range of the FE filter in a 16-bit seismic volume lays between 0 and 32767. High FE values were isolated using opacity filtering to remove all data that were outside the fault geobodies (in our case FE <16000). These high values were subdivided approximately equally as follows: blue (16000-20200), green (20200-24400), yellow (24400-28600) and red (28600-32767). This grouping of FE ranges allowed us to define objects with specific seismic attribute response or seismic fault facies (Iacopini et al., 2012). Tensor, semblance, dip and FE were crossplotted to explore the correlation between these attributes and obtain seismic fault facies. In the study area, as the wells do not directly transect the fault geobodies the seismic fault facies obtained are called “unsupervised” since they contain little to no direct linkage to geological information (Fournier and Derain, 1995). In an attempt to unravel the geological significance of these facies, we compared them to structural properties such as fault throw, dip separation gradient, and juxtaposed lithology (section 4).

3.7 Seismic amplitude versus distance to faults

An analysis of seismic amplitude versus distance to faults was conducted across two regions (~1 x 2 km) within the study area. These regions are not below the gas cloud and were chosen to strictly highlight the area near the end of one fault to the north (area 1), and near the center of the largest fault in the field (area 2). Structural modelling involved populating each of the areas with grid cells (12.5 m, i and j-direction) matching the approximate bin spacing of the seismic data. This cell size was chosen to maintain as much detail in each model as possible. In the depth (k) direction, the cells were also defined to be approximately 12.5 m, where the grid follows the general shape of the interpreted horizons. The volume data of interest was then re-sampled into the grid cells.

The workflow for the amplitude analysis included the following steps: First, we calculated the RMS volume out of the original (non-data conditioned) seismic amplitude data because we were interested in the magnitude of the amplitude rather than its polarity. In order to fit the predefined grid a window size of six traces was chosen to calculate the RMS. Next, the RMS amplitude volume was resampled into the grid. In the resampling, each cell's RMS amplitude value is representative of a weighted interpolation of the amplitudes of the four nearest cells. The grid cells were also populated with distance (m) to fault measurements. Finally, the cells were colored to distinguish three regions on the hanging wall and footwall, which are nearest, central and furthest from the interpreted fault plane.

For each of the five horizons (top Fruholmen to top Kolje), the grid cells were plotted with distance to fault (x-axis) versus normalized RMS amplitude (y-axis). For comparison, the RMS amplitude values for each horizon were then normalized. The points on the crossplots were then colored by the three user defined regions of the hanging wall and footwall. This methodology was also used to analyze how various parameters (e.g. DD and FE) differ with proximity to the fault plane on both the hanging wall and footwall.

4. Results

4.1 Data conditioning

Data conditioning (Fig. 3) resulted in a signal improvement and noise attenuation in specific areas of the seismic volume affected by shallow gas clouds and dolomite (Fig. 5). Figure 5a shows an inline before (left) and after (right) the application of data conditioning. In the original image, the amplitude quality below the gas cloud is low and there is a muffling effect on the signal which is produced by noise. On the data conditioned image, the signal is stronger (normalized) and the noise dimming effect has decreased, especially below the shallow gas cloud. In all other areas (except below the gas cloud), there is a general decrease in noise, which overall improved data signal quality. At the depth range of interpretation (1.5-3 km), data conditioning increased the overall reflector continuity. **INSERT FIGURE 5**

Figure 5b shows a depth slice of the data cube (top) and dip, semblance, tensor and envelope attributes both imaged before (left) and after (right) the data conditioning. In the original amplitude data (Fig. 5b, left), the seismic shows clear amplitude dimming associated with the dolomite and the gas clouds. Both dip and semblance attributes show the effects of the gas clouds (west and north) and the dolomite (northeast, Fig. 5b, left). Tensor and envelope attributes do not show major signs of the gas clouds or dolomite imaging. In the data conditioned seismic (Fig. 5b, right), the amplitude data show greatly improved seismic signal in areas affected by gas clouds and mildly improved imaging in dolomite areas. The dip and semblance depth slices illustrate well the noise reduction below the gas clouds. The noise associated with the gas cloud in the west has almost disappeared, and in the northern gas cloud, the noise has been strongly attenuated but not completely eliminated. There are improvements across the noisy dolomite unit, but they are marginal. Finally, the tensor attribute shows no changes with respect to the gas clouds and dolomite noise, but it shows an overall improvement in the imaging of faults. Since the amplitude is only scaled in areas where gas clouds influence the seismic signal, the envelope attribute is only slightly influenced by the application of data conditioning in these areas.

4.2 Seismic interpretation

Overall, the structure maps indicate the largest fault displacement at the top Fruholmen (oldest) and top Fuglen horizon levels, which is followed by an upwards decrease in displacement from the top Knurr to the top Kolje (youngest, Fig. 6a-e). Three main E-W trending normal fault systems offset the oldest top Fruholmen (Fig. 6e). The northern and central fault systems dip north, while the southern fault system dips south. The northern fault system is segmented into two faults (U and V), with fault U having a smaller NE-SW fault (U') intersecting at the midway point. Fault U intersects constructively fault V in the east. Faults U and V have maximum vertical separation (VS_{max}) of ~180 m and ~290 m respectively. The central fault system is made of three faults, W, X and Y, with VS_{max} of ~100, 150 and 100 m respectively. Faults W and X form a relay. X intersects with Y, and V intersects with Y to form Y' in the east. The southern fault system Z is a laterally extensive system that exhibits a VS_{max} of ~260 m, and complex linkage to the east. Here, fault Z in the south is joined by a smaller south dipping normal fault Z' on its footwall. When referring to the thickness map of the Fruholmen Fm (Fig. 6j), it is clear that this unit is thicker in the west (~290 m) than in the east (~200 m) and sediment thickness is not controlled by faulting (pre-rift sequence). **INSERT FIGURE 6**

The top Fuglen structure map (Fig. 6d) shows the same three main fault systems with the same orientations and linkages. The degree of fault displacement is comparable to the top Fruholmen with the exception of fault U', which is much less prominent. Faults U and V have VS_{max} of ~180 m and 260 m which are respectively the same and less to the same faults for the top Fruholmen. Faults Y' and Z have VS_{max} of 340 and 210 m respectively, these values are smaller to the observed values of the top Fruholmen. The lengths of all faults in the study area do not change drastically in comparison to the top Fruholmen. The complex linkages in the central (W/X relay) and southern (Z-Z') fault systems are clearly visible. The thickness map of the Fuglen Fm (Fig. 6i) also suggests larger sediment accumulation in the west and pre-rift sedimentation.

The shallowest three horizons show significantly less fault displacement, segmentation and linkage. The top Knurr (Fig. 6c) is also displaced by the three main fault systems. However, the degree of fault displacement in this horizon is less than in the top Fuglen. The complexities in fault linkage are therefore less visible. Faults U and V (VS_{max} ~90 and 150 m) are still segmented, but they are shorter in length with respect to the deeper horizons. Faults W, X and Y/Y' still exhibit segmentation, but the relay and fault linkages are less pronounced. Fault Z appears as a single fault extending across the map. VS_{max} of faults Y' and Z are 140 and 120 m respectively, much smaller than the values observed in the deeper horizons. The intra-Kolje (Fig. 6b) shows the same main faults but with much less displacement than in the top Knurr. Fault segmentation is more difficult to establish on the intra-Kolje where VS_{max} <50 m is observed on the northern and southern fault system; the central fault system exhibits slight folding. The top Kolje (Fig. 6a) is the least affected by faulting. Fault segmentation is no longer evident for the northern (U, V) and southern faults (Z, Z') and VS_{max} is <50 m. The central faults (W, X, Y) do not offset this horizon. The thickness maps of the Knurr and Kolje Fms suggest syn-rift sedimentation (Fig. 6f-h).

4.3 Fault throw analysis and quality control

Fault throw was computed using fault cutoffs from the five interpreted horizons (Fig. 7). Fault throw was used to quality control the interpretation. In areas of anomalous throw, changes were made to either horizon or fault interpretations to correct inconsistencies. All major throw anomalies were corrected but small (<20 m) inconsistencies were ignored as they do not affect the overall fault throw distribution. An example of a minor throw anomaly can be seen in the middle of fault U at the top Knurr level, where the cutoffs and the throw undulate (Fig. 7). **INSERT FIGURE 7**

The top Fruholmen and top Fuglen have the largest fault throws across the area (>300 m in Y' and >290 m on fault V; Fig. 7). The top Fruholmen cutoffs exhibit the largest throw values on all faults except fault U, which has its largest throw at the top Fuglen level (~220 m). The largest fault throw maxima in the data volume is observed on fault Y' (>300 m, top Fruholmen). Fault throw follows an elliptical pattern on isolated single faults (W and X relay), and more complex patterns where fault linkages are present (U/V, V/Y, Y/X; Fig. 7). Faults W and X don't vary in throw near their relay (i.e. no suggestion of linkage). At fault intersections, faults transfer displacement: i) fault U transfers displacement to fault V, ii) fault V to fault Y to make the larger displacement fault Y', and iii) fault Y to fault X. For example, at the intersection of U and V, the throws of fault U (~150 m) and fault V (~100 m) are transferred to the southern portion of fault V (~250 m). The same pattern is observed when fault V (~250 m throw) and Y (~50 m throw) intersect and their throws are transferred to Y' (~300 m) east of the intersection.

The top Knurr cutoffs exhibit minimal (50 m or less) throw on faults V and Y and there is no discernible throw on all other faults, so the cutoffs appear to overlap. Fault W does not contain cutoffs for the intra-Kolje and the top Kolje respectively because it doesn't propagate through these shallower units. The top Knurr, intra-Kolje, and top Kolje show <50 m throw on most faults, such that there is a high fault throw gradient (100-200 m) between top Fuglen and top Knurr. This high fault throw gradient results in folding of the three uppermost horizons. We interpret these folds as fault-propagation folds (Withjack et al., 1990; Schlische, 1995; Corfield and Sharp, 2000; Rahman, 2012; Lewis et al., 2015; Paul and Mitra, 2015).

4.4 Dip distortion (DD)

The DD analysis measures fault-related deformation of horizons compared to their regional dip. DD and lateral fault continuity decrease up-section from the top Fruholmen to the top Kolje (Fig. 8). High DD values (>10°, green to red) are associated with faults, while lower values (<10°, blue to green) are linked to more gentle folds. Values below 3° (Fig. 8, dark blue) are considered insignificant. **INSERT FIGURE 8**

The top Fruholmen DD map (Fig. 8e) shows all the main faults and some smaller faults observed in the structure map (Fig. 6e). DD is large (20-30°) and localized along the main faults (U, V, X, Y, Y', Z). Along some of these faults, DD decreases towards the fault tips (U, V, X, Y). For example, fault U has DD values up to 30° in the center of the fault and 10-15° towards the tipline. Fault zone width indicated by high DD is ~500 m (fault Y'), 300 m (faults V and Z), and 100-200 m (faults U, W, X and Y). The faults with the highest throw (V, Y', Z) are also the faults with the largest DD values (>20°), and the widest distortion zones (>300 m). DD also shows that some faults are more laterally extensive than in the structure map. Fault U extends further west and clearly links with the smaller fault U' in the center. Faults W and X are more laterally extensive and enhance hard-linkage at the relay structure (Fig. 8e). The area to the east of fault Z exhibits more complexity than originally interpreted (Fig. 8e, question mark). Here there is likely a small relay structure. With the exception of the hanging wall of fault Z, there is not much folding around the faults. Top Fuglen shows similar DD patterns to the top Fruholmen (Fig. 8d). The main difference in these two maps is that fault X on top Fuglen extends so far northeast that it appears to intersect fault V at a bend. The area to the east of fault Z shows even more complexity at this level, suggesting a fractured relay ramp (Peacock and Sanderson, 1994).

The top Knurr DD map displays an entirely different pattern with respect to the two horizons below (Fig. 8c). DD highlights the three main fault systems, but DD is lower and more dispersed. Overall, faults are more segmented, and fault intersections (e.g. U-V and X-Y) and relays (e.g. W-X) are less apparent. On the hanging wall of the most displaced faults V, Y' and Z, there are wide (~1 km), mid (5-15°) DD areas indicating fault-related folding. Similar, although lower and narrower DD areas are present on the hanging walls of faults U, X and Y.

The central fault system (W-X-Y) is almost imperceptible at the intra-Kolje level (Fig. 8b). Along faults X and Y, there is gentle folding rather than faulting, mostly in the proto-hanging wall areas. In the northern (U-V-Y') and southern (Z) fault systems there is also gentle folding in the hanging wall areas. In the top Kolje DD map (Fig. 8a), only the northern and southern fault systems are visible, and the larger throw faults (Z and Y') are the only ones showing continuity along strike. There is also less folding at this uppermost level than at the intra-Kolje. In general, a comparison of DD values of the top and intra-Kolje to the top Knurr, shows that the faults appear much shorter with shallowing; for example, fault U is >10 km long and ~1 km wide at the top Knurr level, while it is ~8 km long and <500 m wide at the top Kolje. The higher DD values (>30°) are evident for the top Knurr, while lower values (<10°) are more dominant for the intra- and top Kolje. Also, it is more difficult to differentiate individual fault segments in the top and intra-Kolje (e.g. V-Y' or segments along Z).

In summary, top Fruholmen and top Fuglen are mostly offset by the faults, with large and localized DD, while top Knurr has lower, less localized DD and a high component of fault-related folding in the hanging walls. Faulting and folding decrease upwards to the intra-Kolje, in this horizon gentle folds are visible on the hanging walls of the main faults. The top Kolje is only slightly offset or folded (Fig. 8f).

4.5 Seismic attribute analysis

Figure 9 shows the dip, tensor, semblance and envelope attributes, as well as a CMY color blend from the tensor, semblance and dip attributes on the five interpreted horizons. In general, the image quality of the original seismic and therefore the seismic attributes of the lowermost top Fruholmen are the worst. The top Fuglen and top Knurr show the best results with respect to seismic attributes as these display the clearest seismic signal. The contrast in the seismic attributes of the intra-Kolje and top Kolje is the least, as these are less faulted than the deeper horizons. **INSERT FIGURE 9**

Within the various selected attributes, the dip volume is the most successful single attribute for imaging faults in our dataset (Fig. 9a). Upthrown and downthrown fault blocks are visible as dark and light areas, respectively. These coincide with positive and negative dip values. Faults in the top Fruholmen are not well imaged by the dip attribute, while faults in the shallower four horizons are better imaged. The dip response in these horizons weakens upwards from top Fuglen to top Kolje. There is some noise in the three shallowest horizons, which was not removed by data conditioning. This coincides with shallow gas in the north and dolomite in the northeast.

The tensor attribute was the second most successful attribute in imaging faults while keeping noise to a minimum. It provides a high-quality image of faults in the top Fuglen and top Knurr (Fig. 9b). The other three horizons exhibit a weak tensor signal around faults. Unlike the dip cube, the tensor attribute has very little or no noise at all five horizons.

The semblance volume also images the faults relatively well on each horizon (Fig. 9c). Noise caused by shallow gas in the north and dolomite in the northeast is visible at the top Knurr, intra- and top Kolje, and data quality is poor due to random noise at the top Fruholmen. Semblance is the third most successful attribute for imaging faults.

The envelope attribute images the amplitude strength contained in the volume (Taner et al., 1979). The strongest envelope values are present in the top Fuglen and top Knurr depth intervals (Fig. 9d). Fault definition in the tensor, semblance and dip attributes were also strongest at these horizon levels. Therefore, the envelope volume suggests a linkage between the strongest amplitudes and the best fault imaging. Envelope also images gas cloud noise as lower amplitude strengths at the top Fuglen and top Kolje levels.

The CMY color blend of the best three attributes, tensor (Cyan), semblance (Magenta) and dip (Yellow) clearly images faults. When the high values of these attributes overlap (black) the imaged fault displays visible facies (Fig. 9e). The best images are visible on the top Fuglen and top Knurr. There is also some noise in the CMY volume but overall this cube shows the best signal to noise ratio compared to the single attributes.

4.6 Fault enhancement and seismic fault facies

Figure 10 shows the result of the FE analysis in 3D perspective (Fig. 10a), inlines (Fig. 10b-d), and depth slices at the average depth of the interpreted horizons (Fig. 10e-i). In both the inlines and depth slices, the FE maps and the data conditioned seismic are shown. **INSERT FIGURE 10**

Inlines show that the highest FE facies (red) are present at the center of each fault and gradually transition outwards to lower FE facies (yellow to blue). This FE pattern was observed regardless of fault location (Fig. 10a-d). When comparing FE from the western and central parts (Fig. 10b-c) to the eastern part (Fig. 10d), there is an increase in the high FE facies (yellow to red) from west to east. This correlates with higher fault throw and vertical separations to the east (Figs. 6-9). The red to blue seismic fault facies pattern from the center to the edges of the fault zone is also evident in the depth slices (Fig. 10e-i). Similar to the

CMY blend (Fig. 9e), there are seismic quality issues at the average top Fruholmen depth (Fig. 10i), and a decrease of seismic fault facies from top Fuglen to top Kolje (Fig. 10e-h). Faults at the top Fruholmen average depth are poorly imaged, although faults V and Y' (Fig. 6) are relatively well imaged and display high FE facies (yellow to red) at their centers (Fig. 10i). The top Fuglen and top Knurr average depth slices have the highest concentration of seismic fault facies (Fig 10g-h) with the same RYGB outward seismic facies pattern. Also, high FE facies (yellow and red) are more dominant in the east of the field (faults V, Y/Y' and Z; Figs. 6, 10g-h). Along the faults, seismic fault facies are discontinuous. The intra-Kolje and top Kolje average depth slices exhibit low FE facies (green and blue), where green is at the fault center and blue is at the fault edges.

As some noise remained in the data conditioned seismic volume and is visible in the CMY color blend, it affects the FE maps. This noise, which is related to the gas cloud, is visible on the top Fruholmen, top Knurr, intra-Kolje and top Kolje average depth slices as a cloud of high FE values in the central northern part (Fig. 10e-g, i), although it is not conspicuous in the inlines (Fig. 10b-d). Some minor noise associated with the dolomite appears as a fine spotted/mottled texture in the northeast corner of the top Knurr and intra-Kolje (Fig. 10f-g).

Crossplots of attribute data further illustrate the significance of seismic fault facies in terms of the input attributes. In this analysis, we only use data within depths 2110-2750 m, encompassing the top Fuglen and top Knurr, as they offer the best fault images and least noise. Figure 11 a-c shows crossplots of dip-semblance, dip-tensor and tensor-semblance, with the data points colored by the FE facies cutoffs. Semblance is proportional to dip, and FE increases with semblance and dip from the lowest (blue) to the highest (red) facies (Fig. 11a). Tensor is less proportional to dip and there is low correlation between seismic fault facies and tensor (Fig. 11b). Semblance and tensor correlate (as expected in Chopra and

Marfurt, 2005), and seismic fault facies correlate with increasing semblance and to a less degree with increasing tensor. **INSERT FIGURE 11**

The four seismic fault facies are filtered and individually imaged in Fig. 11d-g. The highest FE facies (red) is present across the entire area towards the center of the faults but is focused mostly in the east (Fig. 11d). The yellow facies follows a similar pattern but is farther away from the fault centers (Fig. 11e). The green facies is more widespread across the field area and delimits a wider faulted region than the yellow facies (Fig. 11f). The blue facies is the most laterally and across-fault extensive and is dominant across the entire study area (Fig. 11g).

4.7 Seismic amplitude versus distance to faults

The amplitude versus distance to fault analysis focuses on two smaller areas that have contrasting characteristics with respect to fault throw and related folding. Area 1 is across the northern fault U near its western tipline, while area 2 crosses the center of the largest throw fault Y' (red and yellow rectangles in Fig. 12a, respectively). These areas were investigated by generating horizon-based grids with a series of hanging wall and footwall regions associated with the distance from the interpreted fault plane (Fig. 12b, c). Figure 12d-m shows crossplots of distance to fault versus normalized RMS amplitude for both areas. Each area is separated into hanging wall (left column, red-yellow-blue regions) and footwall (right column, teal-purple-green regions). In the top Fruholmen, top Fuglen and top Knurr, an additional (orange) region indicates cells associated with the fault plane. This region is displayed in the hanging wall crossplots. Best-fit lines for the hanging wall and footwall data illustrate the average trend of amplitudes change approaching the faults. On the right side of Figure 12 (n, o) there are representative seismic inlines which are overlaid with lithology data from the wells (left), or the interpreted fault plane and nearest to furthest regions from it (right). **INSERT FIGURE 12**

In area 1, the top Fruholmen shows a slight decrease in RMS amplitude towards the fault, both from the footwall and hanging wall (Fig. 12h). The intra-fault region (orange) exhibits an increase of amplitude compared to the outermost red region in the hanging wall. The top Fuglen (Fig. 12g) exhibits a slight decrease of amplitude towards the fault from the footwall, and a slight increase of amplitude towards the fault from the hanging wall. The intra-fault region (orange) shows a marked decrease in amplitude. The top Knurr (Fig. 12f) shows a decrease in amplitude towards the fault from the footwall, specifically in the green region near the fault, and an increase of amplitude towards the fault from the hanging wall, especially in the yellow and blue regions closer to the fault. The intra-Kolje (Fig. 12e) exhibits a decrease in amplitude towards the fault from the footwall, a slight increase of amplitude towards the fault in the outermost red and yellow regions of the hanging wall, but a marked decrease in amplitude in the blue region closer to the fault. The top Kolje (Fig. 12d) shows a gradual increase in amplitude towards the fault from the footwall and hanging wall.

Area 2 shows different results. The top Fruholmen (Fig. 12m) shows an increase of amplitude from the footwall, particularly in the green region closest to the fault, a decrease of amplitude from the hanging wall in the red, yellow and blue regions, but a marked increase of amplitude in the intra-fault region (orange). The Top Fuglen (Fig. 12l) has relatively constant amplitude from the footwall, with a slight decrease of amplitude in the green region. From the hanging wall, the amplitude decreases towards the fault, with a sharp decrease in the intra-fault (orange) region. The top Knurr (Fig. 12k) holds the most varied data, the footwall drops in amplitude in the region furthest from the fault (teal) and is constant in amplitude in the next two regions (purple and green). In the hanging wall, the red region shows relative consistency, and then there is a large spike in amplitudes through the yellow and blue regions, followed by a sharp drop in the intra-fault (orange) region. The intra-Kolje (Fig. 12j) shows a gradual increase in amplitude towards the fault from the footwall, and in the hanging wall a slight increase in amplitude through the red region, followed by decreasing amplitude in the yellow and blue regions. The top Kolje (Fig. 12i) exhibits a gradual increase in amplitude towards the fault from the footwall, and in the hanging wall a decrease in amplitude through the red region, followed by an increase in amplitude in the yellow and blue regions. When comparing the two areas, the tops Fruholmen, Fuglen and Knurr show the most severe changes in amplitude, and area 2 shows more extreme amplitude variations.

The N-S seismic inlines for each of the areas (Fig. 12n, o) display folds next to the faults U and Y'. These folds run parallel to the faults and consist of hanging wall synclines and footwall anticlines (with the exception of top Fruholmen, top Fuglen and top Kolje in area 2, which exhibit a hanging wall anticline). These longitudinal folds show reoccurring patterns in the amplitude data. In the hanging wall syncline there is brightening or increase in amplitude towards the fault, while in the footwall anticline there is dimming or decrease in amplitude approaching the fault. In area 1, the shallowest four horizons show synclines in the hanging wall with brightening amplitudes towards the fault, and anticlines in the footwall, which with the exception of top Kolje exhibit dimming amplitudes approaching the fault (Fig. 12d-g). In area 2, despite the presence of hanging wall anticlines, the same pattern is also observed where anticlines correlate with dimming and synclines with brightening amplitudes towards the fault (Fig. 12i-m). These amplitude effects can be traced along strike.

5. Discussion

5.1 Improved seismic imaging and interpretation of faults

The data conditioning workflow (Gilani and Gómez-Martínez, 2013) contributed to a decrease in random and coherent noise as well as increased lateral continuity of reflectors below the shallow gas (Fig. 5). As the workflow is designed to remove the noise caused by shallow gas, it is reasonable that the noise associated with dolomite in the northwest of the study area wasn't completely removed. The application of the workflow in seismically explored areas containing shallow gas (e.g. the southwest Barents Sea) is an excellent way to improve seismic reflector continuity, and therefore fault imaging.

The structure maps (Fig. 6a-e) exhibit a concise summary of interpreted horizons and faults. Since the maps are based on what the geoscientist interprets, they are not always completely representative of all the faults but are a powerful starting point in understanding stratigraphic and structural relationships. In the Snøhvit area, the structure maps show a decrease in fault displacement and lateral extent, as well as less fault connectivity and linkages with shallowing. From the top Knurr and upwards there is decreasing disruption of horizon continuity due to the tipping out of the main faults (Fig. 6a-e). Thickness maps of the five main intervals of interest suggest that the Fruholmen and Fuglen Fms are pre-rift, while the Knurr and Kolje Fms are syn-rift (Fig. 6f-j)

The fault throw analysis (Fig. 7) is also based on the interpretation of faults and horizons surfaces and their intersections (cutoffs). On isolated faults, an elliptical displacement pattern with highest displacement at the center was observed (W, X; Fig. 7). At fault intersections (U/V, V/Y, Y/X; Fig. 7), fault splays transfer displacement to the master faults (U to V, V to Y, and Y to X). Fault intersections or branch lines are generally aligned parallel to the extension direction (Yielding, 2017). In the three fault intersections above, branch lines trend between 014 and 023 (dotted lines, Fig. 6e), which is consistent with N-S extension.

DD (Fig. 8) shows departure of the interpreted horizons from regional dip and is linked to fault related deformation. The highest DD values are present in the deepest top Fruholmen and top Fuglen and decrease upwards. This pattern also applies to the width of the fault zones, which narrow with decreasing depth, to be replaced in the top Knurr and intra-Kolje levels by folding mostly in the hanging walls. These observations are consistent with fault-propagation folding (Withjack et al., 1990; Long and Imber, 2010). The central fault system (W, X, Y) exhibits only slight folding in the intra-Kolje and tips out completely in the top Kolje. This proves that the northern and southern fault systems are larger (and perhaps older) than the central system. DD is also useful for studying the lateral extent of faults. Fault X almost meets fault V in the top Fruholmen and intersects with fault V in the Fuglen DD maps, therefore extending 1.5 km further to the northeast than in the structure maps. Fault interaction at relays is enhanced: for example in the relay between faults X and W, and the complex fractured relay in the eastern portion of fault Z (Fig. 8d-e). DD, however, is limited by the sampling direction. Since the selected transects are N-S, faults with this strike are not imaged in the maps. This is not a major problem in the area where most faults strike E-W.

Seismic attributes also show decreasing faulting, narrowing fault zones, and less prominent fault segments with shallowing (Fig. 9). Dip, tensor and semblance are the most successful attributes in the imaging of faults in this study (Dutzer et al., 2010; Iacopini et al., 2012, 2016). The dip attribute does the best job overall in highlighting the faults. Tensor is successful on the top Fuglen and top Knurr, which have the best reflector image quality, but only manages a subtle image in the less displaced top and intra-Kolje. Semblance clearly images faults on all horizons but is the attribute most susceptible to gas cloud noise. By combining these three attributes into a color blend, it is possible to isolate fault bodies using: reflector orientation (tensor), discontinuity (semblance) and dip. Although seismic attributes do not give the information contained in the structure maps, fault throw and DD analysis, they are an excellent step to apply to a seismic volume before fault interpretation. The creation and usage of a color blend of structure enhancing attributes is a quick and easy way to get started on the interpretation of faults and their relationships on a preliminary basis. Seismic attributes provide the user with images of faults beyond the constraints of human interpretation and are therefore excellent to understand the details contained in the seismic signal surrounding faults.

5.2 The classification of unsupervised seismic fault facies

Unsupervised seismic fault facies were constructed by dividing the high FE values in four classes of increasing value (Fig. 10). The highest FE facies (red) are in the center of faults in the inline and depth slices, and they are more abundant to the northeast of the study area where the faults have the highest throw. Crossplots of seismic attribute data show that with increasing values of semblance, dip and to a minor degree tensor, FE increases (Fig. 11). FE is a relatively simple attribute to highlight faults and their damage zones. However, in order to understand the relationship between the unsupervised seismic fault facies and geological parameters such as fault throw or DD, some more comparisons and further analysis must be incorporated into the study.

FE is a filter that enhances the edges contained in a seismic volume; the magnitude of this measurement is linked to structural deformation. DD is a measurement of apparent dip on interpreted horizons. A comparison of these two measurements may explain the significance of the seismic fault facies with respect to horizon interpretations. This was done for the largest thrown fault (area 2, Fig. 12), where DD and FE data were resampled into the cells of the structural model (Fig. 13b-c). The data are displayed on distance to fault (x-axis) versus normalized RMS amplitude (y-axis) crossplots, but the data points are colored by DD (Fig. 13d-h) and FE (Fig. 13i-m). Due to the nature of the upscaling process of the DD trimeshes into the structural model, it was not possible to populate every cell with DD data. To ensure consistency between the two datasets, the missing points from the DD data clouds were also removed from the FE. In the structural models, it is evident that the highest values of DD and FE are in the three deepest, most offset horizons (Fig. 13 b, c). With the exception of top Fruholmen in the footwall (Fig. 13m), high DD values (>12°) in the top Fruholmen, top Fuglen and top Knurr correlate with the blue to red seismic fault facies, and hanging wall and footwall areas away from the fault show low DD (1-10°) and FE (<16,000) values (Fig. 13f-h and k-m). In the uppermost intra- and top Kolje horizons, there is clear variation in DD (1-10°) mostly in the hanging wall, while the FE is overall low (<16,000; Fig. 13d-e and i-j). Exceptions are the intra-Kolje in the hanging wall where there are blue and green fault facies at ~800 m from the fault, which are related to a small-scale fault, and in the footwall close to the fault where high DD values (>12°) correlate with the blue and green fault facies (Fig. 13j). High DD values in the footwall of top Kolje don’t correlate with the seismic fault facies, suggesting that these values are rather spurious. The four seismic fault facies are thus related to high DD (>12°), while low DD (1-10°) picks up the subtleties of fault related folding.

INSERT FIGURE 13

Long and Imber (2010, 2012) were the original proponent of DD mapping, where the relationship between fault displacement, its gradient and DD was established. We take their comparisons a step further by integrating fault throw, DD, and seismic fault facies. DD and FE classify fault deformation but only DD captures the subtleties associated with fault related folding. Iacopini et al. (2016) used seismic attribute correlation to identify unsupervised seismic fault facies. Botter et al (2016, 2017b) used the FE filter to establish fault facies on synthetic seismic data where a correlation between fault deformation, seismic attribute response, and unsupervised seismic fault facies was established. Our workflow applies these same findings to real seismic data and establishes a methodology for fault interpretation, linking fault throw, DD, seismic attributes and fault facies classification.

To further explore the geological significance of the seismic fault facies, they are compared with fault throw, dip separation gradient and juxtaposed lithology by projecting these attributes onto the fault planes (Fig. 14). The results show a correlation between throw, dip separation gradient and the seismic fault facies (Fig. 14a, b, d). The highest FE facies correlate with the fault areas exhibiting the highest throw, and the highest dip separation gradient (a measure of strain; Fig. 14a, b, d). This result together with the correlation of the seismic fault facies with high DD (Fig. 13), demonstrates a clear link between the seismic fault facies and fault deformation. This is consistent with the findings of Botter et al. (2016, 2017b) in synthetic models. **INSERT FIGURE 14**

As the seismic fault facies are unsupervised, in an attempt to understand their lithological significance, we compared them with the juxtaposed lithology on the faults (Fig. 14c). In the case of a sand dominated lithology, the faults propagated further and offset the sedimentary layers, with the resultant presence of high FE facies (green to red). In the uppermost shale dominated lithologies, the faults tip out, resulting in folding and low FE facies (blue to green). Thus, mechanical stratigraphy controls the distribution of the seismic fault facies in the field.

5.3 Understanding amplitude variations across fault zones

Seismic amplitude versus distance to fault (Fig. 12) proves that a brightening in amplitude occurs when approaching the fault through a syncline, and amplitude dims when approaching the fault through an anticline. This is clearly observed in the less faulted top Knurr, intra and top Kolje (Fig. 12d-f and i-k). In the deeper, more faulted horizons, there can be either dimming or brightening in amplitude towards the fault, although across a narrower distance. In area 1 the Fuglen and area 2 the Fruholmen and Fuglen fms are dominated by sandstones, which may be contributing to the nature of deformation evident in these sections and therefore the amplitude distributions (lithology data in wells; Fig. 12 n, o). The top Knurr, intra and top Kolje are all associated with shales, which may play a key role in the formation of anticlines and synclines in these units (Fig 12, n, o). In the top Fuglen (area 1, 2) and the top Knurr (area 2), the results are conclusive with a major decrease in amplitude on the fault (Fig. 12 k, g, l, orange regions). The deepest horizon (top Fruholmen) is inconsistent with observed systematic amplitude patterns in both areas. In area 1, there is an increase in amplitude associated with the fault plane (Fig. 12h, orange region) but on further inspection it is clear that this is due to a second poorly-imaged subsidiary fault, slightly south of the main interpreted fault (Fig. 12, n). In area 2, the top Fruholmen also exhibits increasing amplitudes associated with the fault plane (Fig. 12m, orange region). Here, there may be another subsidiary fault influencing reflector continuity, although with the low signal/noise ratio of the data at this depth (Fig. 12o) this is difficult to define. There are several explanations for the observed changes in amplitude across faults:

a. *Geometrical focusing and defocusing of the seismic signal caused by reflector curvature-* Relative to a flat plane, the reflected seismic energy is spread over a larger surface when the reflection occurs on an anticline, and over a smaller surface in the presence of a syncline (Sheriff and Geldart, 1995). The resulting seismic will exhibit stronger reflections associated with synclines (focusing), and weaker reflections (defocusing) in the case of anticlines (Sheriff and Geldart, 1995). This effect is related to a geometry parameter.
b. *Acoustic properties-* Changes to the acoustic properties of a rock occur when the rock undergoes structural deformation (Couples et al., 2007; Skurtveit et al., 2013). Previous

studies have modelled fault zones and found that changing acoustic properties associated with fault related deformation results in amplitude variations (Botter et al., 2014, 2016). This is most likely in the high FE facies associated to large deformation (yellow and red, Fig. 10 orange region Fig 11, 12k-m). However, without access to well cores or logs of these rocks, it is not possible to prove if this correlation exists.

c. *Survey Geometry/ Illumination mapping* – The seismic data are controlled by the geometry and acquisition direction of the seismic survey (Laurain et al., 2004; Drottning et al., 2006; Gjøystdal et al., 2007). Several studies document that illumination direction also has an effect on the measured seismic amplitudes especially with respect to faults (Drottning et al., 2006; Gjøystdal et al., 2007; Lecomte, 2008; Botter et al., 2014, 2016; Lecomte et al., 2015). The seismic data used in this study are the near-angle stacks (5-20°) of a data cube merged from five 3D streamer surveys. The specifics of the merged survey are not equivalent to the single surveys and therefore it is difficult to quantify the effect shooting direction has on seismic amplitude. It would be an interesting study to explore how illumination direction affects the imaging of structural geometry (i.e. curving the reflectivity surface) and its effect on the seismic amplitude.

5.4 Implications

A common practice for interpreting faults in seismic data is to pick fault sticks on seismic lines (Caine et al., 1996; Faulkner et al., 2010). This is then followed by the construction of faults planes (from the interpolation of fault sticks). When comparing the structure maps (Fig. 6) to the throw (Fig. 7), DD (Fig. 8), and FE (Fig. 10) maps, it is evident that these additional properties help to provide a wealth of information regarding fault extent, displacement patterns and linkage. Having a greater understanding of these three parameters can improve the interpreter's knowledge of fault connectivity, fault seal potential, flow and pressure barriers, top seal integrity, and the mapping of mega sequences (pre-, syn- and post rift). Specifically, DD (Fig. 8) gives a more conclusive understanding of the lateral and vertical extent of faults, fault connectivity and the presence of small (even sub-seismic) scale faults. The application of the FE filter on any structure enhancing attribute volume, or a combination of these attributes, results in a volume where faults are highlighted and easy to interpret. FE (Fig. 10) allows for a more conclusive understanding of the lateral and vertical extent of faults, fault internal structure, and fault facies classification, as it seems that FE correlates with fault deformation. FE, however, is not a great indicator of the subtleties associated with fault-related folding. Seismic attributes (Fig. 9) are also a quick and simple way to understand fault structure in a seismic volume, but a CMY color blend of multiple attributes gives a clearer image of faults for interpretation. In the essence of time, anyone of these properties or their combination can lead to a better understanding of fault formation, linkage, and amplitude anomalies near fault planes. This is not only important for the petroleum industry, but for any industry interested in understanding the geophysical and geological impact of faults.

A brightening and dimming effect towards the fault was witnessed in the seismic amplitudes analysis of this paper. Variations in seismic amplitude near fault planes can be related to seismic signal focusing, changes in acoustic properties, and/or illumination effects from seismic acquisition (Badley, 1985; Sheriff and Geldart, 1995; Laurain et al., 2004; Couples et al., 2007; Skurtveit et al., 2013), all of which are potentially related to the structural geometry of the surface imaged. With limited lithologic control it is difficult to infer the effects lithological variation has on the variations in amplitude witnessed here. In order to analyze the reason for seismic brightening and dimming more accurately, it is necessary to acquire a dataset where wells are transecting a fault plane.

We analyzed a near-angle stack focusing on PP reflections. Future work will involve analysis of ocean bottom seismic (OBS) data from the Snøhvit Field to compare how PP and PS data signals differ with respect to fault characterization.

Acknowledgements

The authors would like to thank the Norwegian Ministry of Education and Research for funding this research. Equinor ASA and their partners in the Snøhvit Field, Petoro AS, Total E&P Norge AS, Neptune Energy Norge AS and Dea Norge AS provided the seismic data for this work. We would also like to thank Schlumberger (Petrel), Geoteric (Geoteric) and Badley's (T7) for providing us with academic licenses of their softwares, and for their support.

References

Aarland, R.K., Skjerven, J., 1998. Fault and fracture characteristics of a major fault zone in the northern North Sea: Analysis of 3D seismic and oriented cores in the Brage Field (Block 31/4). Geological Society, London, Special Publications 127, 209–229.

Alaei, B., 2016. Seismic attributes and their application in seismic interpretation.

Ashcroft, W., 2011. A Petroleum Geologists Guide to Seismic Reflection, 1st ed. Wiley-Blackwell.

Badley, M., 1985. Practical Seismic Interpretation. Boston, USA.

Bakker, P., 2002. Image structure analysis for seismic interpretation. Technische Universiteit Delft.

Barnes, A.E., 2000. Attributes for automating seismic facies analysis. SEG 70th Annual International Meeting. 553–556.

Barnett, J.A.M., Mortimer, J., Rippon, J.H., Walsh, J.J., Watterson, J., 1987. Displacement geometry in the volume containing a single normal fault. AAPG Bulletin 71, 925–937.

Berglund, L.T., Augustson, G., Færseth, R., Ramberg-Moe, H., 1986. The evolution of the Hammerfest Basin, Habitat of Hydrocarbons on the Norwegian Continental Shelf. Graham & Trotman for the Norwegian Petrolium Society.

Botter, C., Cardozo, N., Hardy, S., Lecomte, I., Escalona, A., 2014. From mechanical modeling to seismic imaging of faults: A synthetic workflow to study the impact of faults on seismic. Marine and Petroleum Geology.

Botter, C., Cardozo, N., Hardy, S., Lecomte, I., Paton, G., Escalona, A., 2016. Seismic characterization of fault damage in 3D using mechanical and seismic modelling. Marine and Petroleum Geology 77, 973–990.

Botter, C., Cardozo, N., Lecomte, I., Rotevatn, A., Paton, G., 2017a. The impact of faults and fluid flow on seismic images of a relay ramp over production time. Petroleum Geoscience 23, 17–28.

Botter, C., Cardozo, N., Qu, D., Tveranger, J., Kolyukhin, D., 2017b. Fault damage zones seismic characterization of fault facies models. Interpretation 5, 1–18.

Caine, J.S., Evans, J.P., Forster, C.B., 1996. Fault zone architechture and permeability structure. Geology 24, 1025–1028.

Carcione, J.M., Herman, G.C., ten Kroode, A.P.E., 2002. Seismic Modeling. Geophysics 67, 1304–1325.

Childs, C., Manzocchi, T., Walsh, J.J., Bonson, C.G., Nicol, A., Schöpfer, M.P.J., 2009. A geometric model of fault zone and fault rock thickness variations. Journal of Structural Geology 31, 117–127.

Childs, C., Watterson, J., Walsh, J.J., 1995. Fault overlap zones within developing normal fault systems. Journal of the Geological Society 152, 535–549.

Chopra, S., Marfurt, K.J., 2007. Seismic Attributes for Prosepct Identification and Reservoir Characterization. Society of Exploration Geophysicists and European Association of Geoscientists and Engineers, Tulsa, OK, United States of America.

Chopra, S., Marfurt, K.J., 2005. Seismic attributes - A historical perspective. Geophysics 70, 3SO–28SO. https://doi.org/10.1190/1.2098670

Corfield, S., Sharp, I.R., 2000. Structural style and stratigraphic architecture of fault propagation folding in extensional settings: A seismic example from the Smorbukk area, Halten Terrace, Mid-Norway. Basin Research 12, 329–341. https://doi.org/10.1111/j.1365-2117.2000.00133.x

Couples, G., Ma, J., Lewis, H., Olden, P., Quijano, J., Fasae, T., Maguire, R., 2007. Geomechanics of faults: impacts on seismic imaging. First Break 83–90.

Dalland, A., Worsley, D., Ofstad, K., 1988. A lithostratigraphic scheme for the Mesozoic and Cenozoic succession offshore mid- and northern Norway., Norwegian Petroleum Directorate Bulletin.

Doré, A.G., 1995. Barents Sea Geology, Petroleum Resources and Commercial Potential. Arctic 48, 207–221.

Drottning, Å., Lecomte, I., Gjøystdal, H., Skorstad, A., Kolbjørnsen, O., Huseby, O., 2006. Modelling the seismic response to production: a closer look at the sensitivity to overburden, survey, rock physics model and seismic modelling approach. NPF-Seminar Kristiansand 1–4.

Dumay, J., Fournier, F., 1988. Multivariate statistical analyses applied to seismic facies recognition. Geophysics 53, 1151–1159.

Dutzer, J.-F., Basford, H., Purves, S., 2010. Investigating fault-sealing potential through fault relative seismic volume analysis. Petroleum Geology Conference Series 7, 509–515.

Eichhubl, P., D'Onfro, P.S., Aydin, A., Waters, J., McCarty, D.K., 2005. Structure, petrophysics, and diagenesis of shale entrained along a normal fault at Black Diamond Mines, California - Implications for fault seal. AAPG Bulletin 89, 1113–1137.

Elliott, G.M., Wilson, P., Jackson, C. a. L., Gawthorpe, R.L., Michelsen, L., Sharp, I.R., 2012. The linkage between fault throw and footwall scarp erosion patterns: An example from the Bremstein Fault Complex, offshore Mid-Norway. Basin Research 24, 180–197.

Færseth, R.B., Johnsen, E., Sperrevik, S., 2007. Methodology for risking fault seal capacity: Implications of fault zone architecture. AAPG Bulletin 91, 1231–1246.

Faulkner, D.R., Jackson, C.A.L., Lunn, R.J., Schlische, R.W., Shipton, Z.K., Wibberley, C.A.J., Withjack, M.O., 2010. A review of recent developments concerning the structure, mechanics and fluid flow properties of fault zones. Journal of Structural Geology 32, 1557–1575.

Fournier, F., Derain, J., 1995. A statistical methodology for deriving reservoir properties from seismic data. Geophysics 60, 1437–1450.

Gauthier, B.D.M., Lake, S.D., 1993. Probabilistic modeling of faults below the limit of seismic resolution in Pelican Field, North Sea, offshore United Kingdom. AAPG Bulletin 77, 761–777.

Gilani, S.F., Gómez-Martínez, L., 2013. The application of data conditioning, frequency decomposition and DHI from RGB colour blending in the Gohta discovery (Barents Sea, Norway). First Break 33, 39–45.

Gjøystdal, H., Iversen, E., Lecomte, I., Kaschwich, T., Drottning, Å., Mispel, J., 2007. Improved applicability of ray tracing in seismic acquisition, imaging, and interpretation. Geophysics 72, SM261-SM271.

Iacopini, D., Butler, R., Purves, S., McArdle, N., De Freslon, N., 2016. Exploring the seismic expression of fault zones in 3D seismic volumes. Journal of Structural Geology 89, 54–73.

Iacopini, D., Butler, R.W.H., 2011. Imaging deformation in submarine thrust belts using seismic attributes. Earth and Planetary Science Letters 302, 414–422.

Iacopini, D., Butler, R.W.H., Purves, S., 2012. Seismic imaging of thrust faults and structural damage: A visualization workflow for deepwater thrust belts. First Break 30, 77–84.

Landa, E., 2012. Seismic diffraction: where’s the value? SEG Technical Program Expanded Abstracts 1–4.

Landa, E., 2007. Beyond Conventional Seismic Imaging. EAGE.

Landa, E., Keymar, S., 1998. Seismic monitoring of diffraction images for detection of local heterogeneities. Geophysics 63, 1093–1100.

Laurain, R., Vinje, V., Strand, C., 2004. Simulated migration amplitude for improving amplitude estimates in seismic illumination studies. The Leading Edge 23, 240.

Lecomte, I., 2008. Resolution and illumination analyses in PSDM: A ray-based approach. Leading Edge (Tulsa, OK) 27, 650–663.

Lecomte, I., Lavadera, P.L., Anell, I., Buckley, S.J., Schmid, D.W., Heeremans, M., 2015. Ray-based seismic modelling of geologic models: Understanding and analyzing seismic images efficiently. Interpretation 3, SAC71-SAC89.

Lewis, M.M., Jackson, C.A.L., Gawthorpe, R.L., Whipp, P.S., 2015. Early synrift reservoir development on the flanks of extensional forced folds: A seismic-scale outcrop analog from the Hadahid fault system, Suez rift, Egypt. AAPG Bulletin 99, 985–1012.

Linjordet, A., Olsen, R.G., 1992. The Jurassic Snøhvit gas field, Hammerfest basin, offshore northern Norway. Giant Oil and Gas Fields of the Decade 1978-1988. 349–370.

Long, J.J., Imber, J., 2012. Strain compatibility and fault linkage in relay zones on normal faults. Journal of Sedimentary Petrology 36, 16–26.

Long, J.J., Imber, J., 2011. Geological controls on fault relay zone scaling. Journal of Structural Geology 33, 1790–1800.

Long, J.J., Imber, J., 2010. Geometrically coherent continuous deformation in the volume surrounding a seismically imaged normal fault-array. Journal of Structural Geology 32, 222–234.

Marfurt, K.J., 2006. Robust estimates of 3D reflector dip and azimuth. Geophysics 71, P29.

Marfurt, K.J., Kirlin, R.L., Farmer, S.L., Bahorich, M.S., 1998. 3-D seismic attributes using semblance-based coherency algorithm. Geophysics 63, 1150–1165.

Ostanin, I., Anka, Z., di Primio, R., Bernal, A., 2012. Identification of a large Upper Cretaceous polygonal fault network in the Hammerfest basin: Implications on the reactivation of regional faulting and gas leakage dynamics, SW Barents Sea. Marine Geology 332–334, 109–125.

Paul, D., Mitra, S., 2015. Fault patterns associated with extensional fault-propagation folding. Marine and Petroleum Geology 67, 120–143.

Peacock, D.C.P., Sanderson, D.J., 1994. Geometry and development of relay ramps in normal fault systems. AAPG Bulletin 78, 147–165.

Posamentier, H., Kolla, V., 2003. Seismic geomorphology and stratigraphy of depositional elements in deep-water settings. Journal of Sedimentary Research 73, 367–388.

Purves, S., Basford, H., 2011. Visualizing geological structure with subtractive color blending. In: Marfurt, K.J., Gao, D., Barnes, A., Chopra, S., Corrao, A., Hart, B., James, H., Pacht, J., Rosen, N.C. (Eds.), Attributes: New Views on Seismic Imaging -- Their Use in Exploration and Production: 31st Annual. SEPM Society for Sedimentary Geology, 120–139.

Rahman, J., 2012. Compactions, rock Properties Evalulation, rock physics diagnostics, AVO modelling and seismic inversion in the Snohvit Field, SW Barents Sea. University of Oslo.

Rippon, J.H., 1985. Contoured patterns of the throw and hade of normal faults in the Coal Measures (Westphalian) of north-east Derbyshire. Proceedings of the Yorkshire Geological Society 45, 147–161.

Schlische, R.W., 1995. Geometry and origin of fault-related folds in extensional settings. AAPG Bulletin 79, 1661–1678.

Sheriff, R.E., Geldart, L.P., 1995. Exploration Seismology, 2nd ed. Cambridge University Press, Cambridge.

Shuey, R.T., 1985. A simplification of the Zoeppritz equations. Geophysics 50, 609–614.

Skurtveit, E., Torabi, A., Gabrielsen, R.H., Zoback, M.D., 2013. Experimental investigation of deformation mechanisms during shear-enhanced compaction in poorly lithified sandstone and sand. Journal of Geophysical Research: Solid Earth 118, 4083–4100.

Sund, T., Skarpnes, O., Nørgård Jensen, L., Larsen, R.M., 1984. Tectonic development and hydrocarbon potential offshore Troms, Northern Norway. AAPG Special Publication Memoir: Future Petroleum Provinces of the World. 615–627.

Taner, M.T., Koehler, F., Sheriff, R.E., 1979. Complex seismic trace analysis. Geophysics 44, 1041–1063.

Townsend, C., Firth, I.R., Westerman, R., Kirkevollen, L., Harde, M., Andersen, T., 1998. Small seismic-scale fault identification and mapping. Geological Society, London, Special Publications 147, 1–25.

Widess, M.B., 1973. How thin is a thin bed? Geophysics 38, 1176–1180.

Wilson, P., Elliott, G.M., Gawthorpe, R.L., Jackson, C. a. L., Michelsen, L., Sharp, I.R., 2013. Geometry and segmentation of an evaporite-detached normal fault array: 3D seismic analysis of the southern Bremstein Fault Complex, offshore mid-Norway. Journal of Structural Geology 51, 74–91.

Wilson, P., Hodgetts, D., Rarity, F., Gawthorpe, R.L., Sharp, I.R., 2009. Structural geology and 4D evolution of a half-graben: New digital outcrop modelling techniques applied to the Nukhul half-graben, Suez rift, Egypt. Journal of Structural Geology 31, 328–345.

Withjack, M.O., Olson, J., Peterson, E., 1990. Experimental models of extensional forced folds. AAPG Bulletin 74, 1038–1054.

Yielding, G., 2017. The geometry of branch lines. Geological Society, London, Special Publications. 11 LP-22.

Yielding, G., Freeman, B., 2016. 3-D Seismic-Structural Workflows – Examples Using the Hat Creek Fault System. In: Krantz, B., Ormand, C., Freeman, B. (Eds.), M111: 3-D Structural Interpretation: Earth, Mind and Machine. 155–171.

Figure Captions

Figure 1. a. Geologic setting of the Hammerfest Basin. The area in b is marked by a black box. Modified from NPD Factmaps. b. Snøhvit Field area. The dashed yellow line shows the extent of seismic data and the orange rectangle is the study area. Map modified from Linjordet and Olsen (1992) and Ostanin et al. (2012). The blue background of the map refers to the Jurassic Hammerfest Basin while the red shapes on the map identify the areal extents of lower-middle Jurassic gas fields. c. Generalized lithostratigraphic column of the Barents

Sea highlighting the horizons of interest. Modified from Ostanin et al. (2012). d. North-south seismic line through the middle of the study area (X-X' in b) with interpreted horizons and faults. Interpreted horizons are: A: top Kolje, B: intra-Kolje, C: top Knurr, D: top Fuglen, and E: top Fruholmen.

Figure 2. Workflow used in this study.

Figure 3. Data conditioning (noise attenuation and amplitude normalization) workflow used to remove the noise associated to the gas clouds and the northeast dolomite unit.

Figure 4. Fault throw and dip distortion (DD). a. 3D image of a normal fault showing displacement field and hanging wall and footwall cutoffs, fault length and width. b. Map view of a fault with trim and patch distances used in the cutoffs determination. c. Cross section explaining the calculation of DD.

Figure 5. Results of data conditioning. a. Inline 2745 before (left) and after (right) data conditioning. The gas cloud (~500 m) imaged on the inline causes poor amplitude distribution in deeper reflectors. This is improved by data conditioning. b. Seismic amplitude, dip, semblance, tensor and envelope attribute slices at 2300 m depth, before (left) and after (right) data conditioning. Improved noise attenuation associated with the gas clouds (red circles) and a thick dolomite unit (yellow circle) is clear in the dip and semblance attributes.

Figure 6. Structure maps of the five interpreted horizons and vertical thickness maps calculated using distance between tops. a. Top Kolje (youngest). b. Intra-Kolje, c. Top Knurr, d. Top Fuglen, and e. Top Fruholmen (oldest). U-Z' are faults. Dotted lines in e are the branch lines for the fault intersections UV, VY and YX. For comparison, a 500 m elevation range color bar is adjusted to a medial depth for each horizon. Vertical thickness maps of f. top-intra Kolje, g. intra-Kolje-top Knurr, h. Knurr Fm, i. Fuglen Fm, and j. Fruholmen Fm.

All thickness maps are displayed on a color bar of 0-400 m. Wells 1-4 are included for reference on all structure and thickness maps. The contour interval for all maps is 25 m.

Figure 7. Fault throw distribution on main fault planes. This was used to understand fault linkage and to quality control interpretations. Inset shows the faults on the top Fruholmen structure map.

Figure 8. Dip distortion (DD) of the a. Top Kolje, b. Intra-Kolje, c. Top Knurr, d. Top Fuglen, and e. Top Fruholmen. f. 3D view of DD. On each horizon, DD is calculated along N-S transects spaced every 100 m and is projected to the average horizon elevation.

Figure 9. a. Dip, b. Tensor, c. Semblance, d. Envelope, and e. Cian-magenta-yellow (CMY) color blend combining tensor (C), semblance (M) and dip (Y) attributes on the top Kolje (first column), intra-Kolje (second column), top Knurr (third column), top Fuglen (fourth column), and top Fruholmen (fifth column).

Figure 10. Fault enhancement (FE) and comparison to seismic cube. a. Selected inlines and depth slices colored by five FE ranges: white is no fault, and blue to red are four unsupervised seismic facies within the fault zones. b, c and d are inline slices (3502, 2982 and 2473 respectively) of FE (top) and the data conditioned amplitude (bottom). e-i are depth slices of FE (left) and the data conditioned amplitude (right) at the average depth of the top Kolje (1800 m), intra-Kolje (2100 m), top Knurr (2300 m), top Fuglen (2400 m) and top Fruholmen (2750 m).

Figure 11. a. Dip versus semblance, b. Dip versus tensor, and c. Tensor versus semblance of fault zone areas (FE >16,000) in the interval between top Knurr and top Fuglen. In a-c, points are color coded by the four FE facies in Fig. 10. d-g. The four seismic fault facies displayed as geobodies on the selected depth interval.

Figure 12. Seismic amplitude versus distance to faults. a. Top Fuglen map showing areas 1 and 2 (red and yellow rectangles respectively). Area 1 is 2300 m long, 900 m wide and ranges from 1700-2800 m depth. Area 2 is 2300 m long, 900 m wide and ranges from 1900-2800 m depth. b. Structural model of area 1. c. Structural model of area 2. Both models are viewed from the northwest and their cells are colored as hanging wall (red to orange) and footwall (teal to green) regions. d-h. Area 1 hanging wall (left) and footwall (right) crossplots of distance to fault versus RMS amplitude (window size = 6) for the top Kolje, intra-Kolje, top Knurr, top Fuglen and top Fruholmen, respectively. i-m. Similar crossplots for area 2.

Figure 13. a. Top Fuglen map showing area 2 (yellow rectangle). b. Structural model of area 2 with dip distortion (DD) resampled into the grid cells. c. Structural model of area 2 with FE resampled into the grid cells. Both models are viewed from the northwest. d-h. Hanging wall (left) and footwall (right) crossplots of distance to fault versus RMS amplitude (window size = 6) with data points colored by DD for the top Kolje, intra-Kolje, top Knurr, top Fuglen and top Fruholmen, respectively. i-m. Same crossplots but with data points colored by FE.

Figure 14. a. Fault throw, b. Dip separation gradient, c. Juxtaposed lithology, and d. FE (seismic fault facies) along main faults in the area.

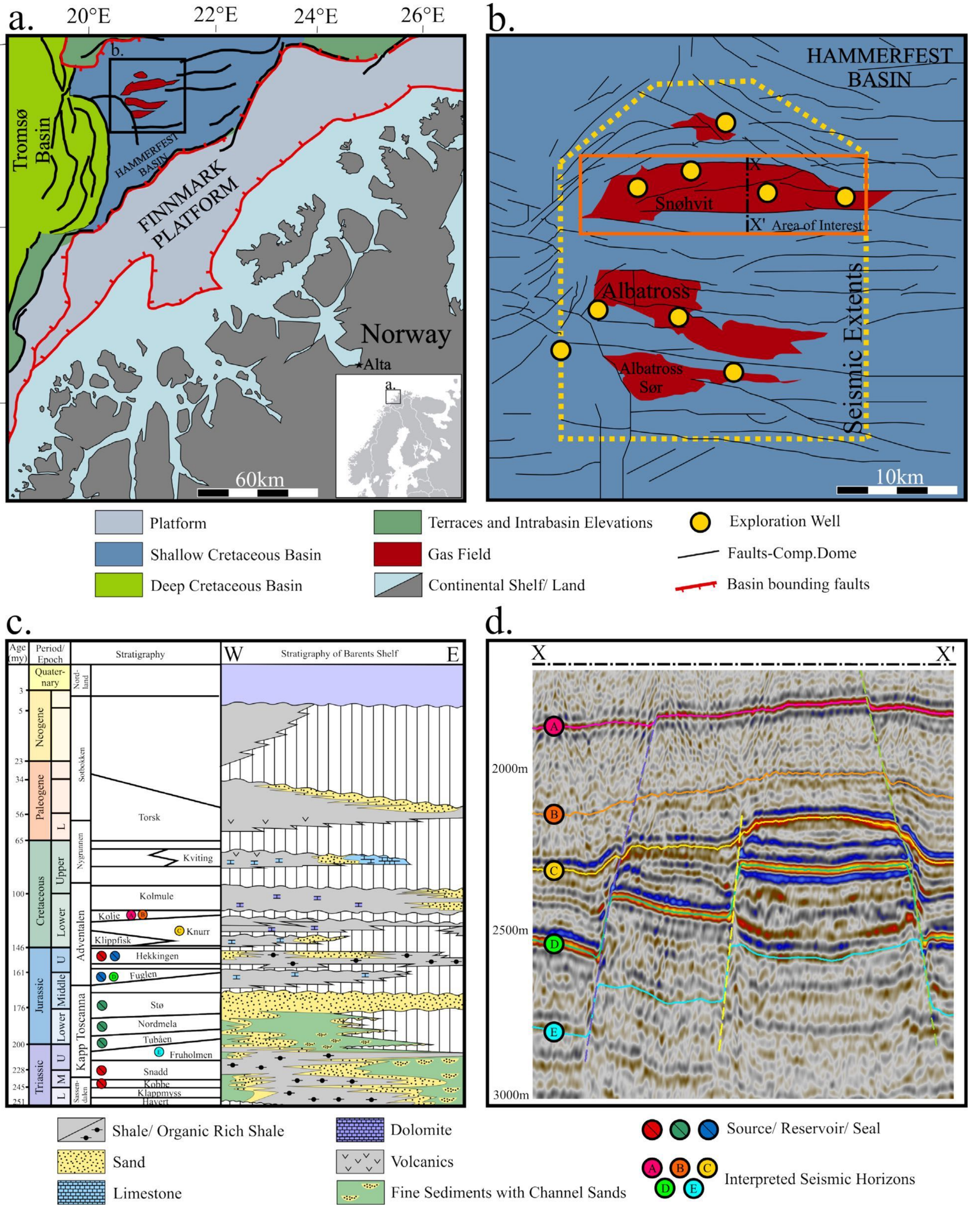

a.
20°E
22°E
24°E
26°E
72°N
71°N
70°N
b.
Tromsø Basin
HAMMERFEST BASIN
FINNMARK PLATFORM
Norway
Alta
a.
60km
b.
HAMMERFEST BASIN
X
X'
Snøhvit
Area of Interest
Albatross
Albatross Sør
Seismic Extents
10km
Platform
Shallow Cretaceous Basin
Deep Cretaceous Basin
Terraces and Intrabasin Elevations
Gas Field
Continental Shelf/ Land
Exploration Well
Faults-Comp.Dome
Basin bounding faults
c.
Age (my)
Period/ Epoch
Stratigraphy
W
Stratigraphy of Barents Shelf
E
Quaternary
Neogene
Paleogene
Cretaceous
Jurassic
Triassic
Upper
Lower
Middle
U
M
L
Nordland
Sotbakken
Nygrunnen
Adventalen
Kapp Toscanna
Sassendalen
Torsk
Kviting
Kolmule
Kolje
Knurr
Klippfisk
Hekkingen
Fuglen
Stø
Nordmela
Tubåen
Fruholmen
Snadd
Kobbe
Klappmyss
Havert
3
5
23
34
56
65
100
146
161
176
200
228
245
251
d.
X
X'
2000m
2500m
3000m
A
B
C
D
E
Shale/ Organic Rich Shale
Sand
Limestone
Dolomite
Volcanics
Fine Sediments with Channel Sands
Source/ Reservoir/ Seal
Interpreted Seismic Horizons

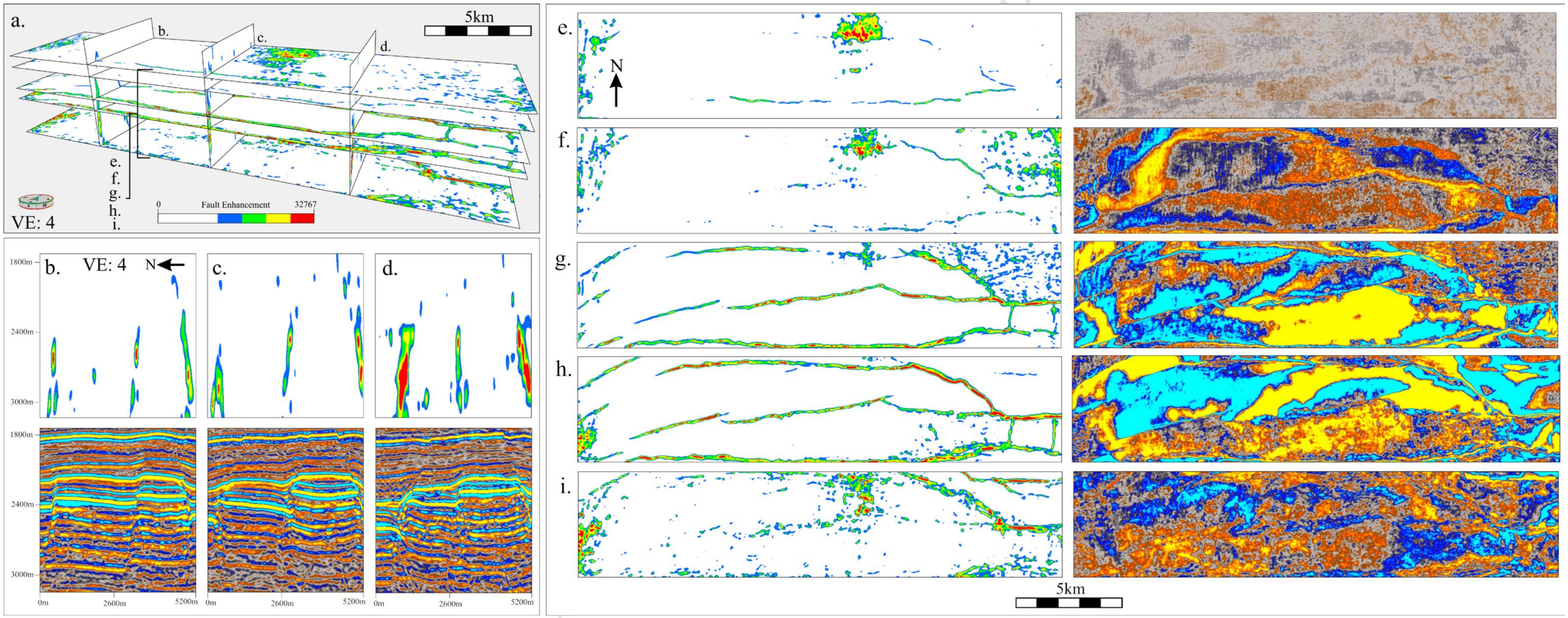

a.
5km
b.
c.
d.
e.
f.
g.
h.
i.
VE: 4
0
Fault Enhancement
32767
b.
VE: 4
N
c.
d.
1800m
2400m
3000m
0m
2600m
5200m
e.
f.
g.
h.
i.
N
5km

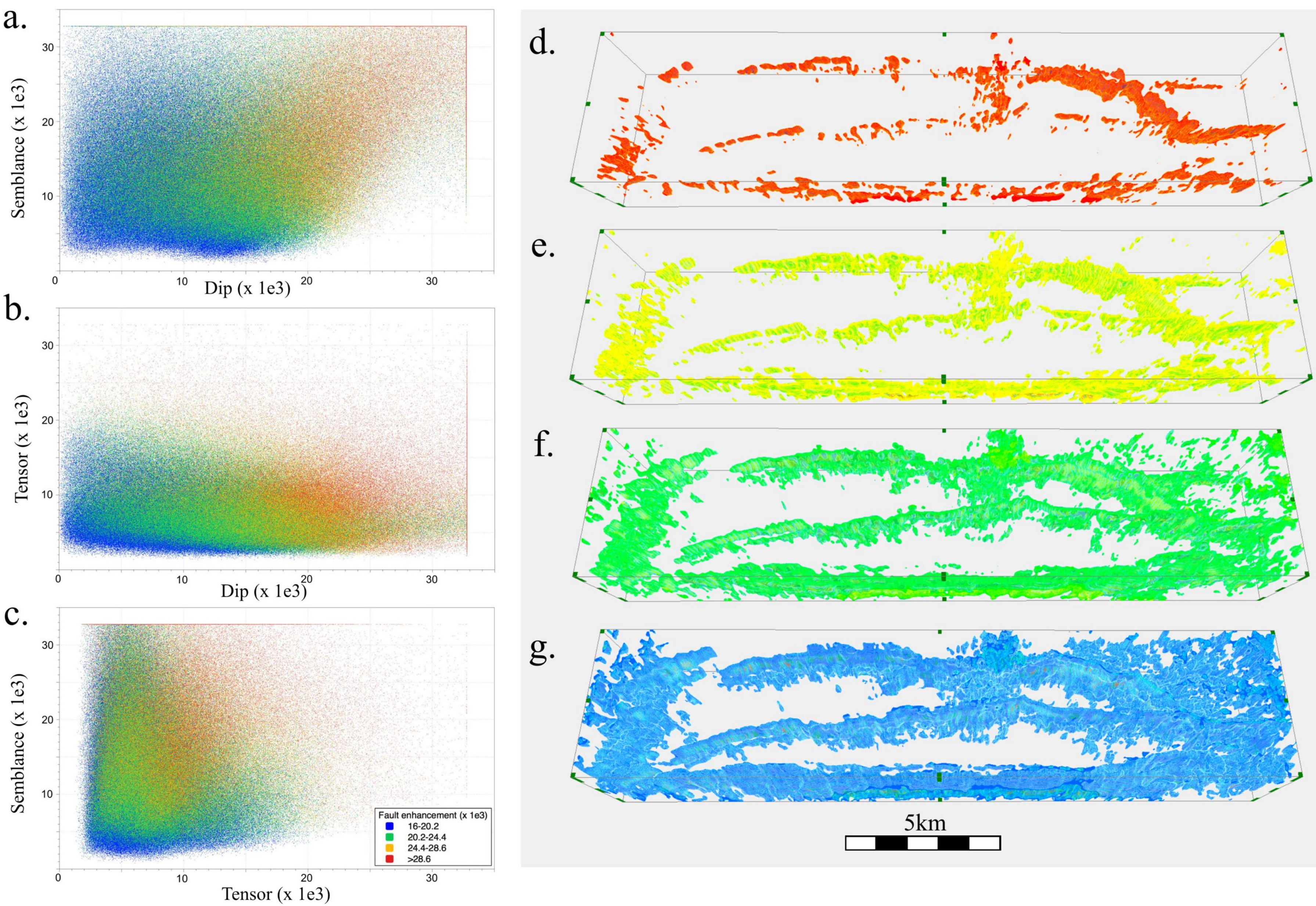
a.
Semblance (x 1e3)
Dip (x 1e3)
b.
Tensor (x 1e3)
Dip (x 1e3)
c.
Semblance (x 1e3)
Tensor (x 1e3)
Fault enhancement (x 1e3)
16-20.2
20.2-24.4
24.4-28.6
>28.6
d.
e.
f.
g.
5km

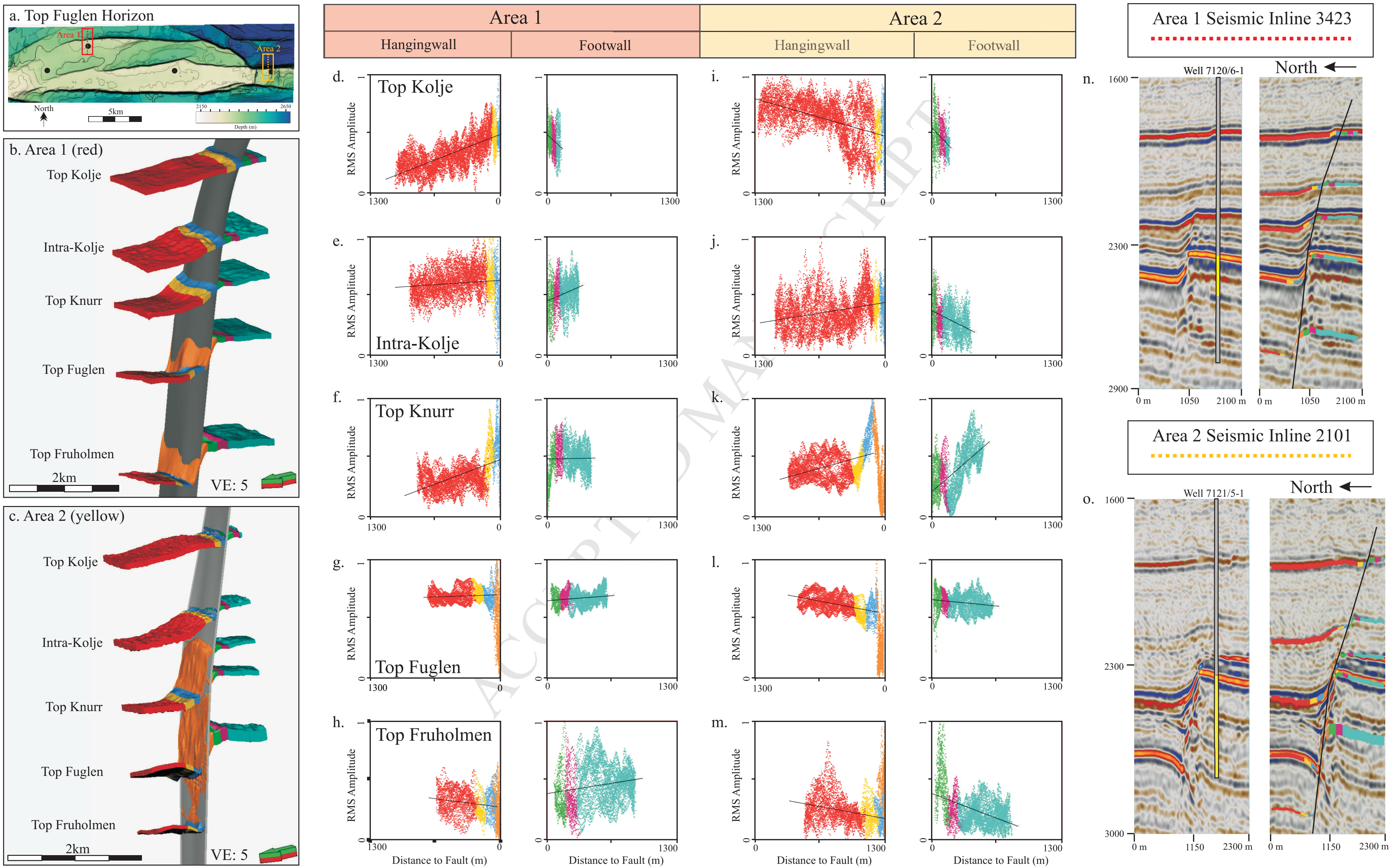

a. Top Fuglen Horizon
Area 1
Area 2
North
5km
2150
2650
Depth (m)
b. Area 1 (red)
Top Kolje
Intra-Kolje
Top Knurr
Top Fuglen
Top Fruholmen
2km
VE: 5
c. Area 2 (yellow)
Top Kolje
Intra-Kolje
Top Knurr
Top Fuglen
Top Fruholmen
2km
VE: 5
Area 1
Area 2
Hangingwall
Footwall
Hangingwall
Footwall
d.
Top Kolje
e.
Intra-Kolje
f.
Top Knurr
g.
Top Fuglen
h.
Top Fruholmen
i.
j.
k.
l.
m.
RMS Amplitude
Distance to Fault (m)
1300
0
Area 1 Seismic Inline 3423
Well 7120/6-1
North
n.
1600
2300
2900
0 m
1050
2100 m
Area 2 Seismic Inline 2101
Well 7121/5-1
North
o.
1600
2300
3000
0 m
1150
2300 m

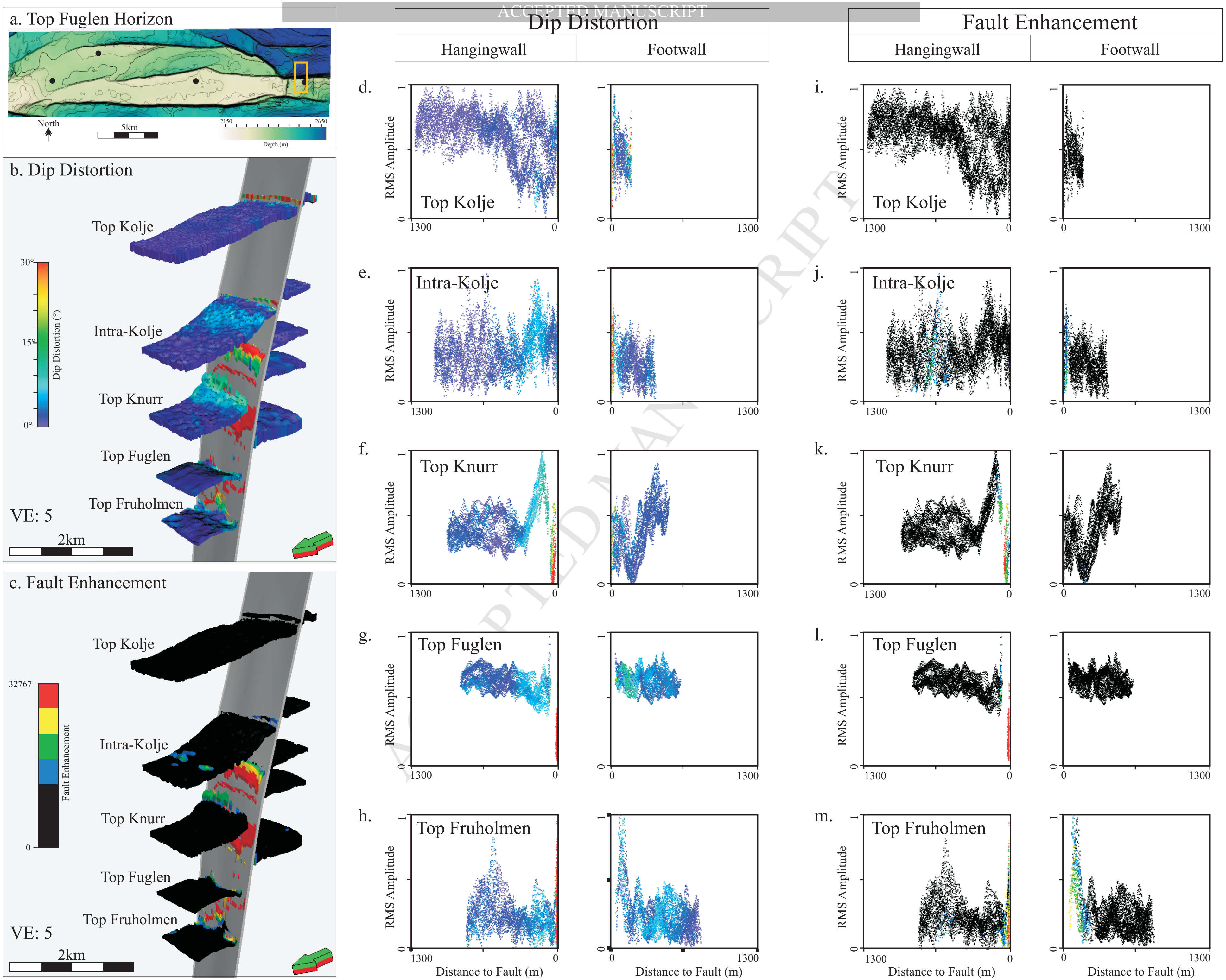

a. Top Fuglen Horizon
North
5km
2150
2650
Depth (m)
b. Dip Distortion
Top Kolje
Intra-Kolje
Top Knurr
Top Fuglen
Top Fruholmen
30°
15°
0°
Dip Distortion (°)
VE: 5
2km
c. Fault Enhancement
Top Kolje
Intra-Kolje
Top Knurr
Top Fuglen
Top Fruholmen
32767
0
Fault Enhancement
VE: 5
2km
Dip Distortion
Hangingwall
Footwall
Fault Enhancement
Hangingwall
Footwall
d.
e.
f.
g.
h.
i.
j.
k.
l.
m.
Top Kolje
Intra-Kolje
Top Knurr
Top Fuglen
Top Fruholmen
RMS Amplitude
1300
0
Distance to Fault (m)

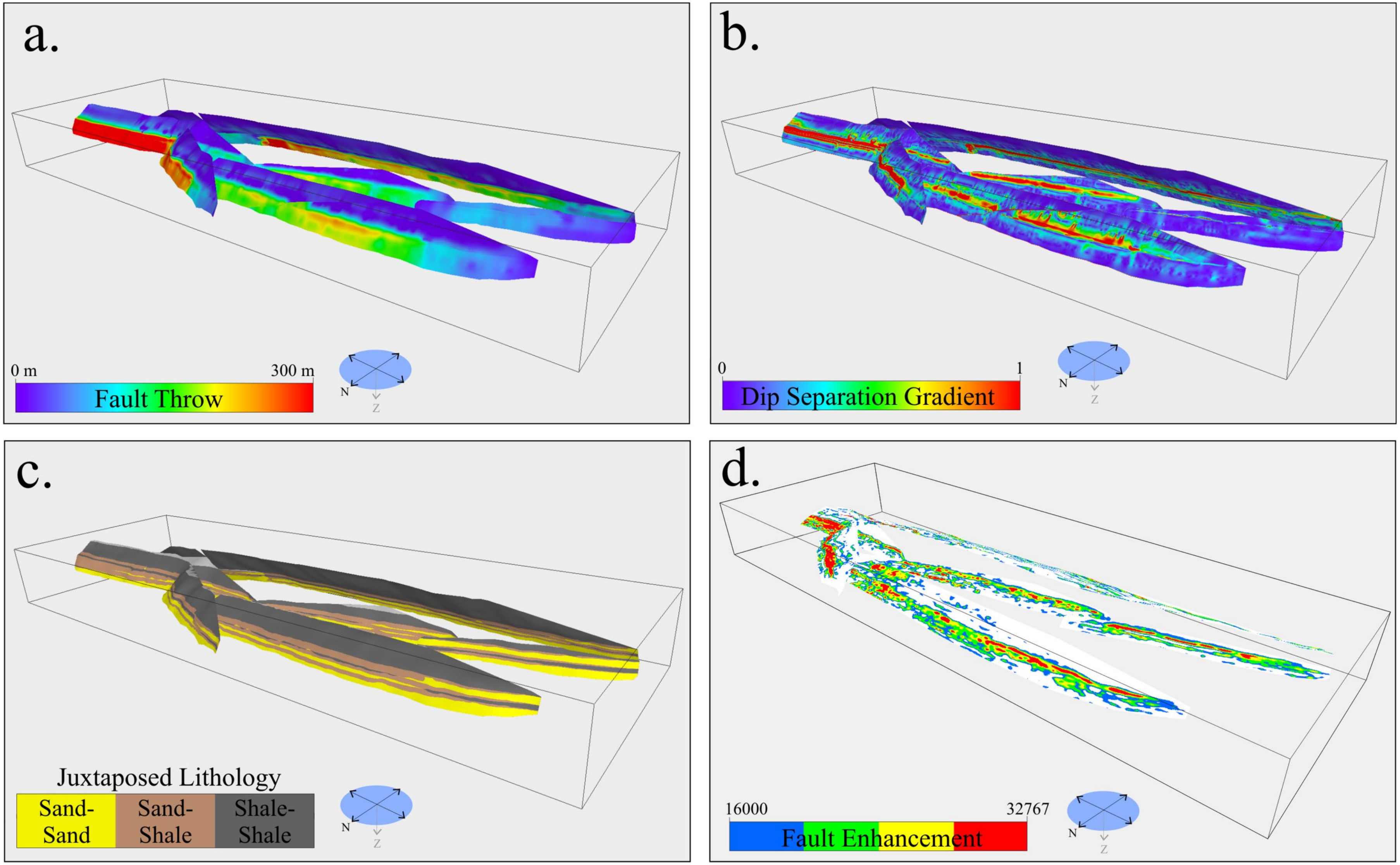
a.
0 m
300 m
Fault Throw
N
Z
b.
0
1
Dip Separation Gradient
N
Z
c.
Juxtaposed Lithology
Sand-Sand
Sand-Shale
Shale-Shale
N
Z
d.
16000
32767
Fault Enhancement
N
Z

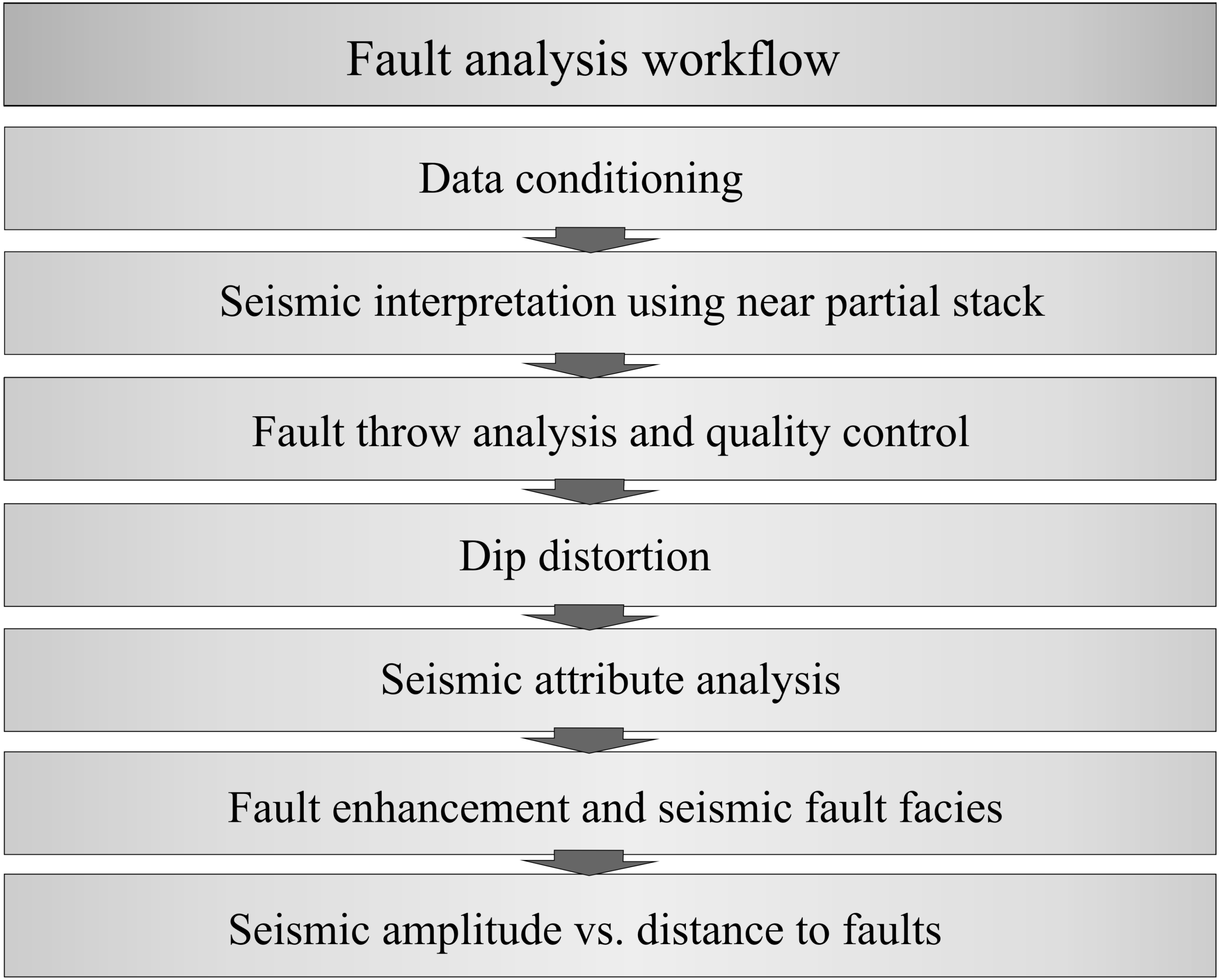
Fault analysis workflow
Data conditioning
Seismic interpretation using near partial stack
Fault throw analysis and quality control
Dip distortion
Seismic attribute analysis
Fault enhancement and seismic fault facies
Seismic amplitude vs. distance to faults

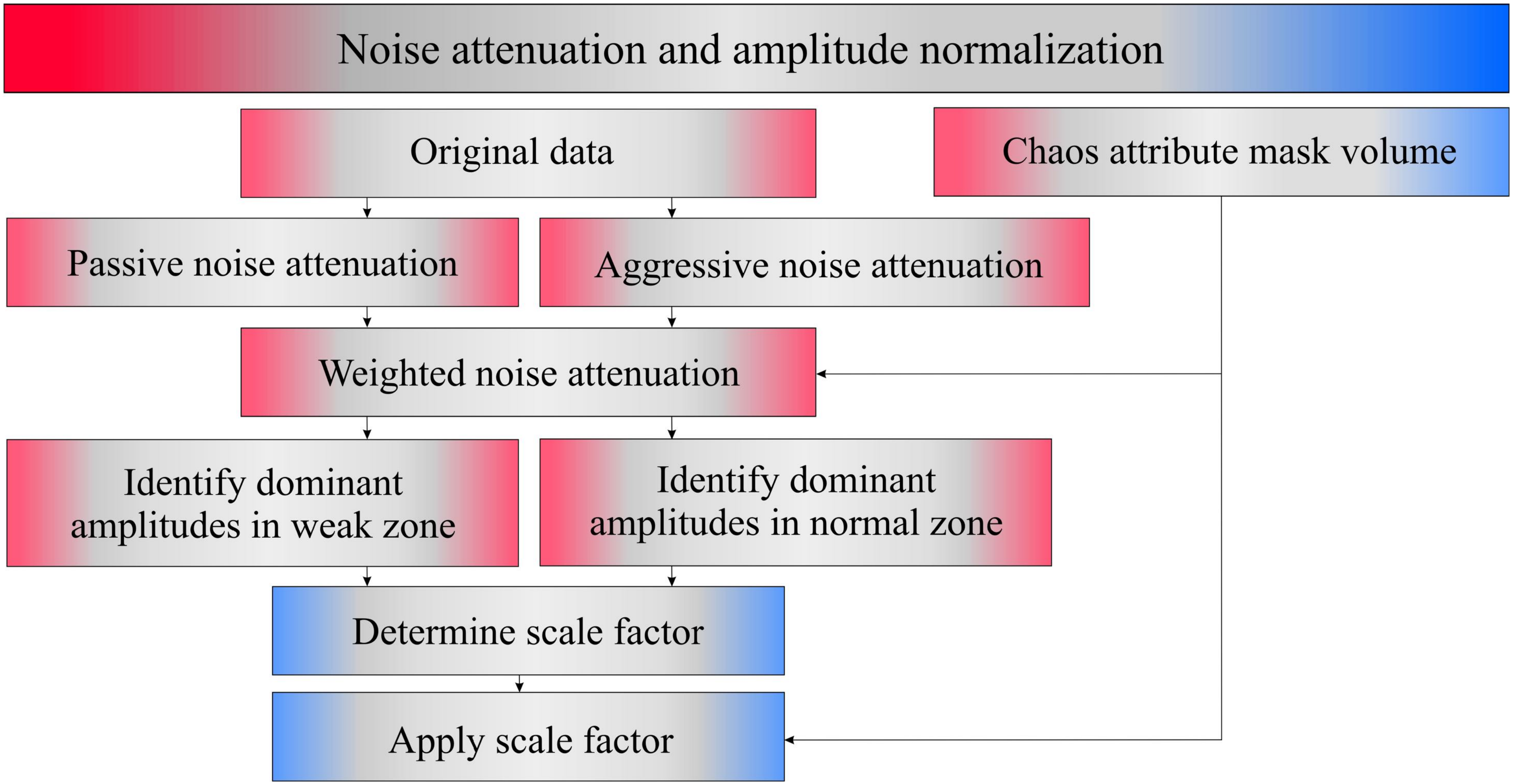
Noise attenuation and amplitude normalization
Original data
Chaos attribute mask volume
Passive noise attenuation
Aggressive noise attenuation
Weighted noise attenuation
Identify dominant amplitudes in weak zone
Identify dominant amplitudes in normal zone
Determine scale factor
Apply scale factor

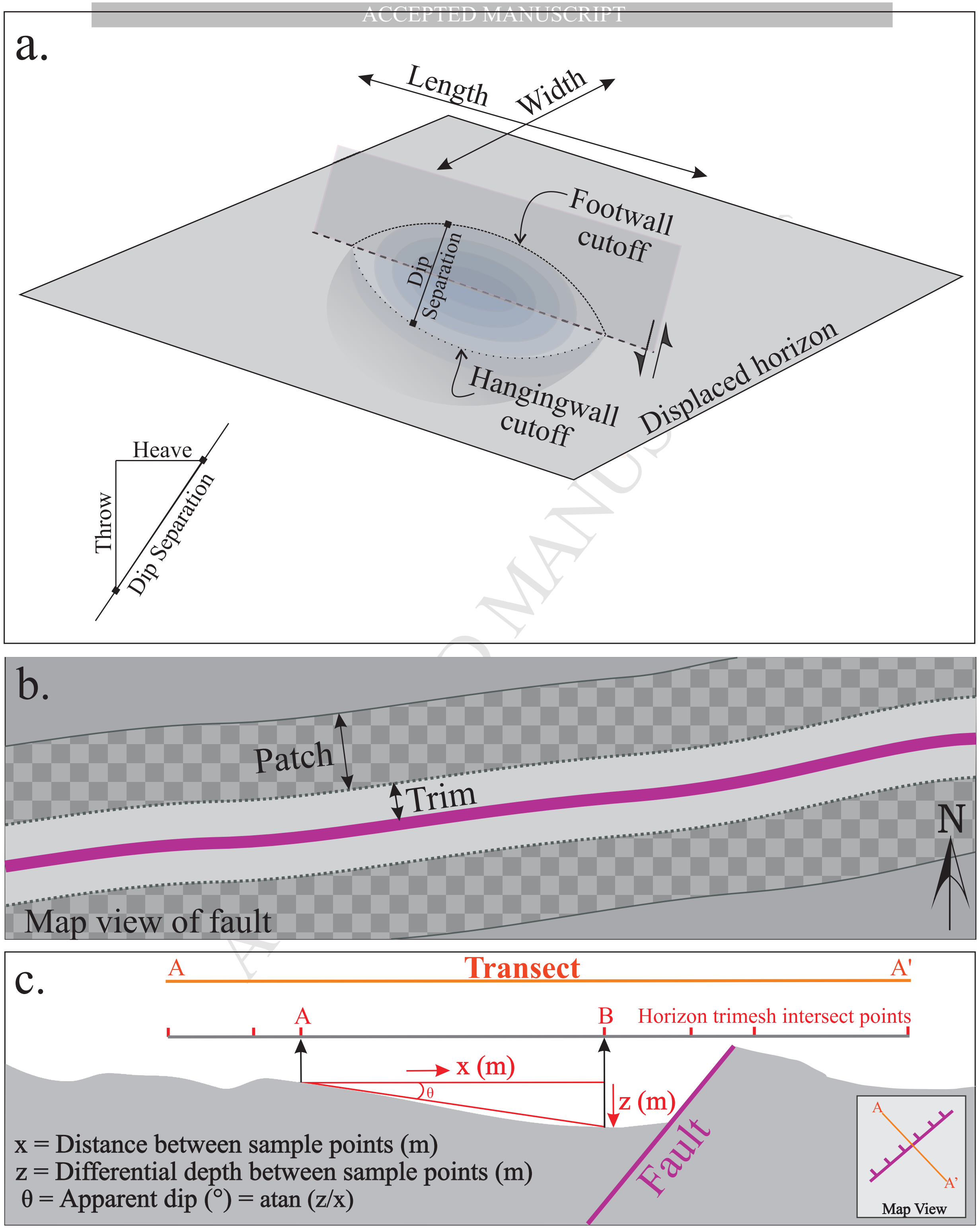

a.
Length
Width
Footwall
cutoff
Dip
Separation
Hangingwall
cutoff
Displaced horizon
Heave
Throw
Dip Separation
b.
Patch
Trim
N
Map view of fault
c.
A
Transect
A'
A
B
Horizon trimesh intersect points
x (m)
θ
z (m)
Fault
x = Distance between sample points (m)
z = Differential depth between sample points (m)
θ = Apparent dip (°) = atan (z/x)
A
A'
Map View

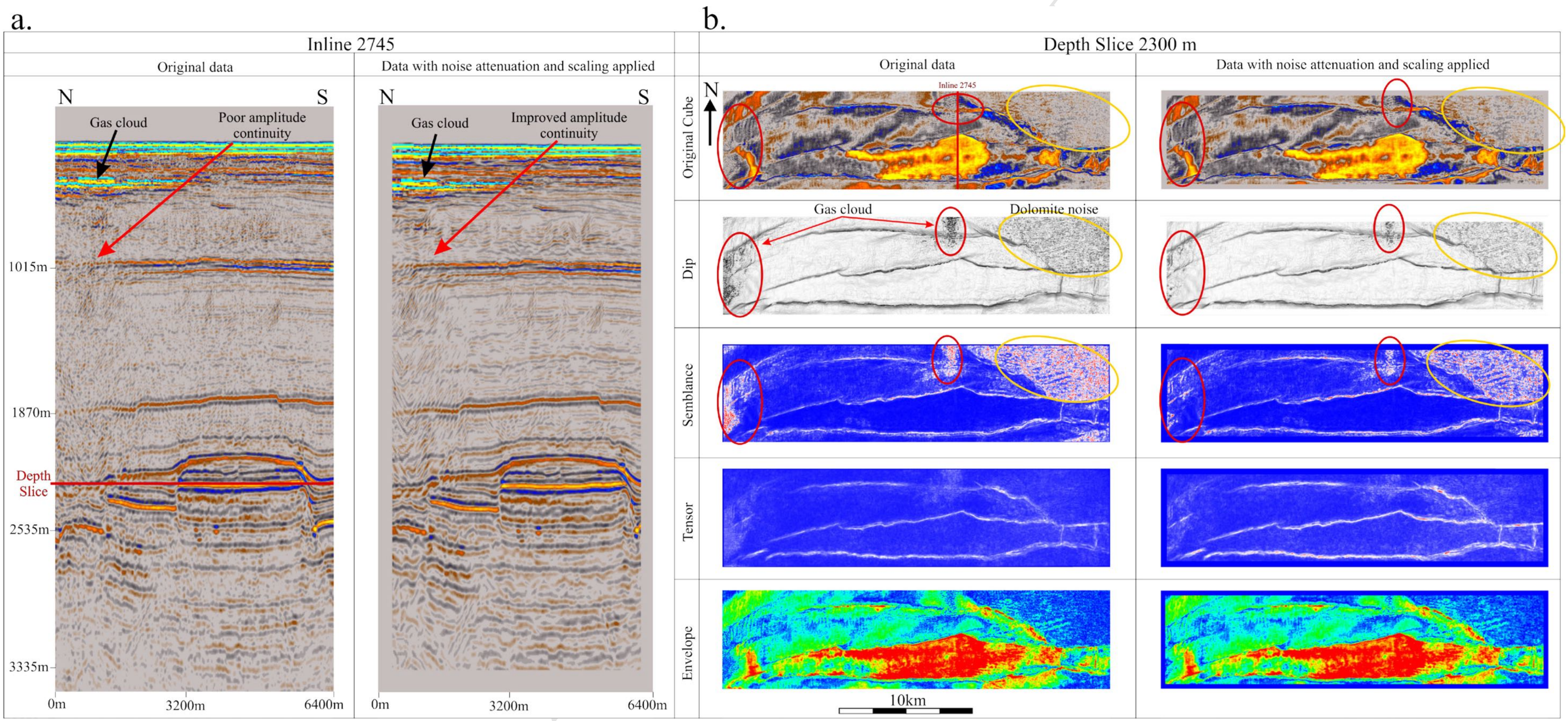
a.
b.
Inline 2745
Original data
Data with noise attenuation and scaling applied
N
S
Gas cloud
Poor amplitude continuity
Improved amplitude continuity
1015m
1870m
Depth Slice
2535m
3335m
0m
3200m
6400m
Depth Slice 2300 m
Original Cube
Inline 2745
Dip
Gas cloud
Dolomite noise
Semblance
Tensor
Envelope
10km

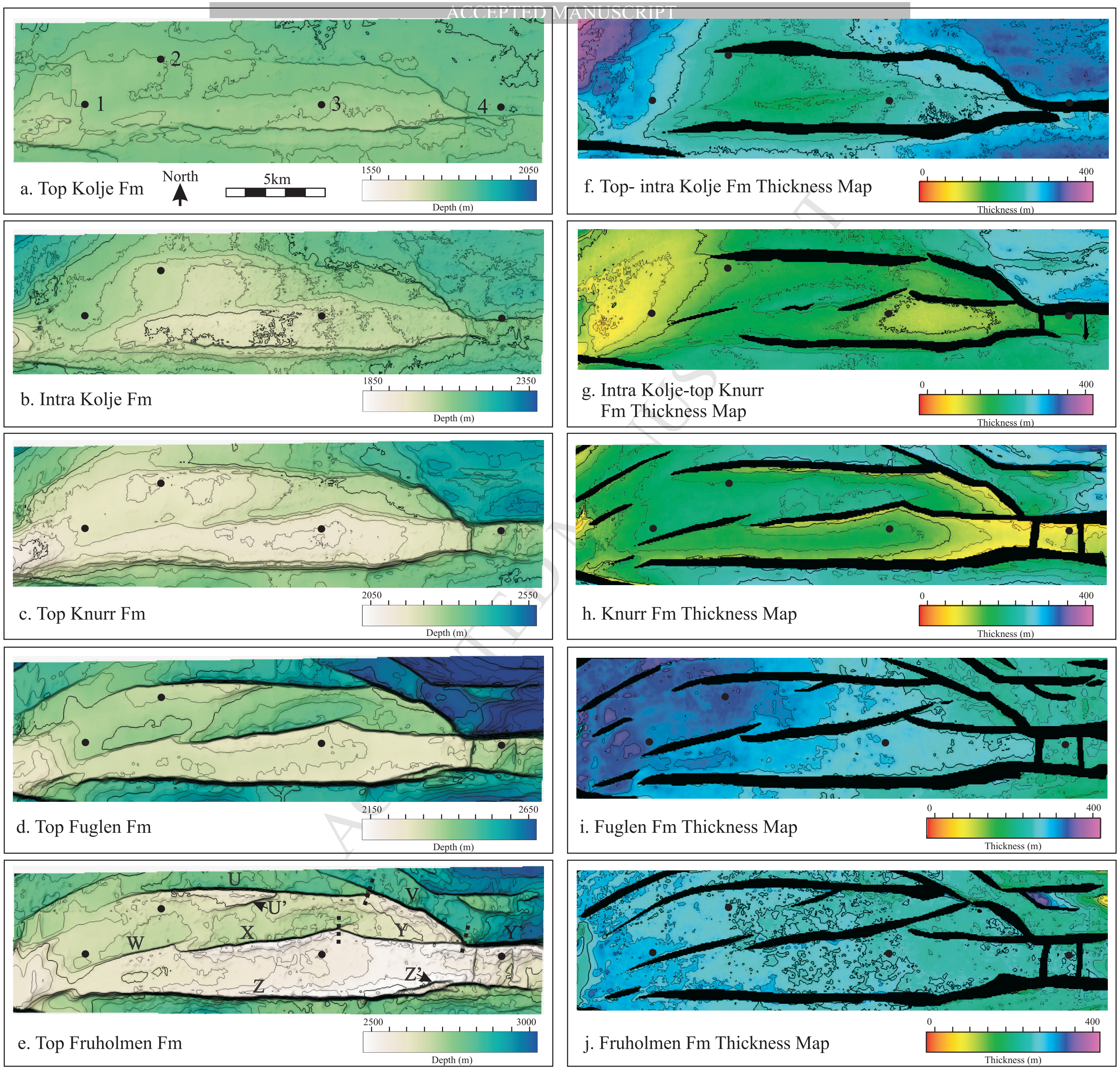

2
1
3
4
a. Top Kolje Fm
North
5km
1550
2050
Depth (m)
f. Top- intra Kolje Fm Thickness Map
0
400
Thickness (m)
b. Intra Kolje Fm
1850
2350
Depth (m)
g. Intra Kolje-top Knurr Fm Thickness Map
0
400
Thickness (m)
c. Top Knurr Fm
2050
2550
Depth (m)
h. Knurr Fm Thickness Map
0
400
Thickness (m)
d. Top Fuglen Fm
2150
2650
Depth (m)
i. Fuglen Fm Thickness Map
0
400
Thickness (m)
U
U'
V
W
X
Y
Y'
Z
Z'
e. Top Fruholmen Fm
2500
3000
Depth (m)
j. Fruholmen Fm Thickness Map
0
400
Thickness (m)

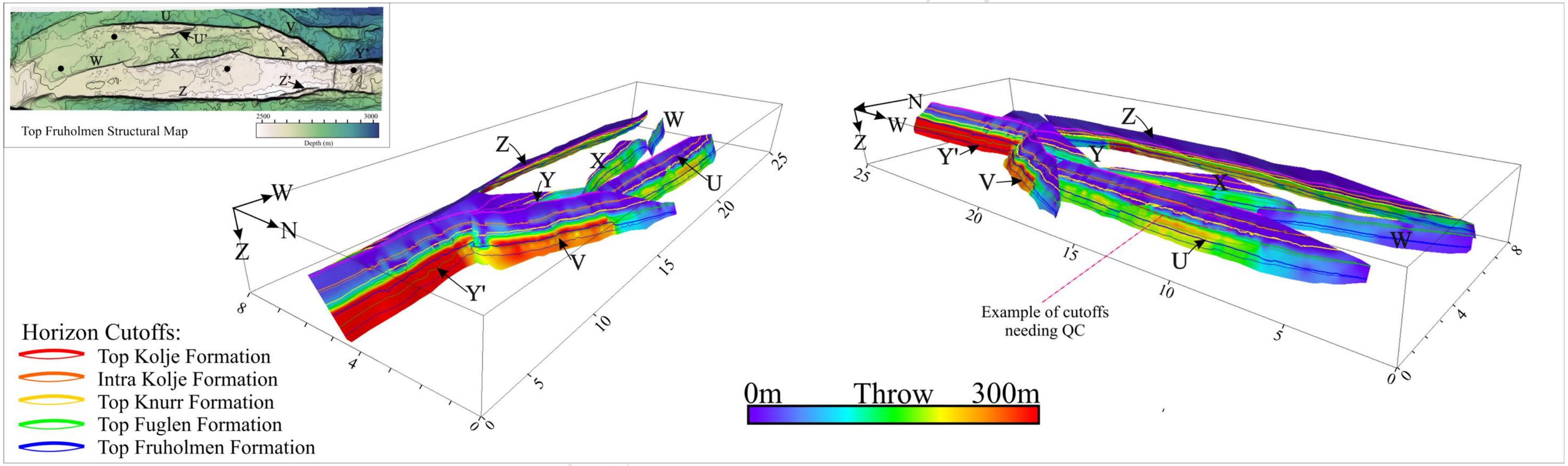

U
U'
V
W
X
Y
Y'
Z
Z'
Top Fruholmen Structural Map
2500
3000
Depth (m)
Z
W
X
U
Y
W
N
Z
V
Y'
8
4
0
0
5
10
15
20
25
N
W
Z
Y'
Y
Z
V
X
W
U
25
20
15
10
5
8
4
0
0
Example of cutoffs needing QC
0m
Throw
300m
Horizon Cutoffs:
Top Kolje Formation
Intra Kolje Formation
Top Knurr Formation
Top Fuglen Formation
Top Fruholmen Formation

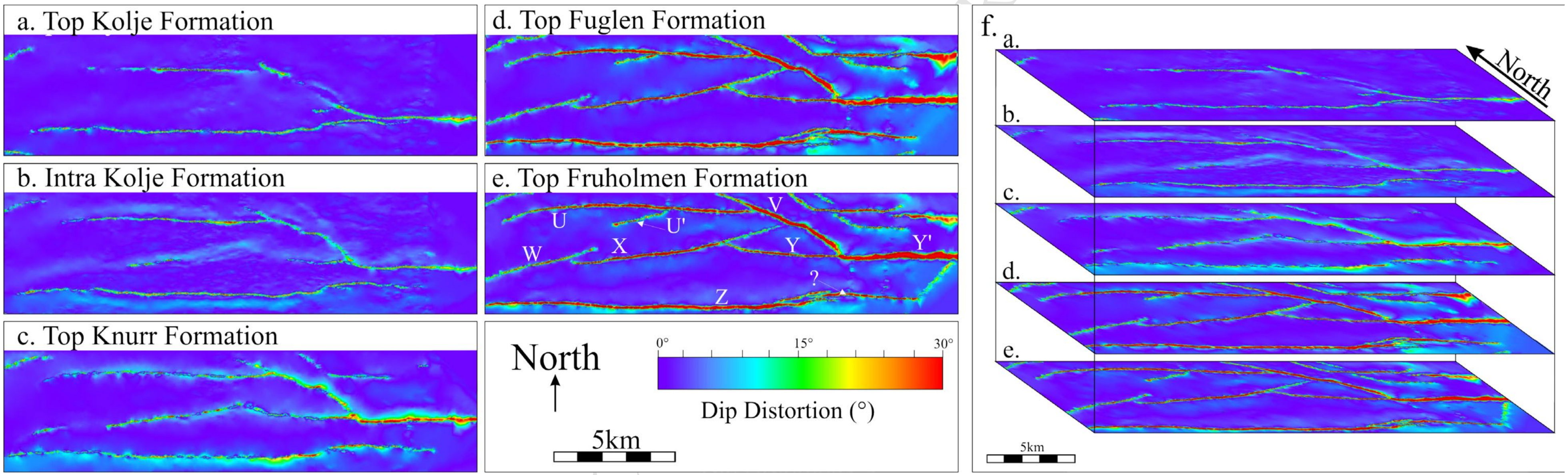
a. Top Kolje Formation
b. Intra Kolje Formation
c. Top Knurr Formation
d. Top Fuglen Formation
e. Top Fruholmen Formation
U
U'
V
W
X
Y
Y'
?
Z
North
0°
15°
30°
Dip Distortion (°)
5km
f.
a.
b.
c.
d.
e.
North
5km

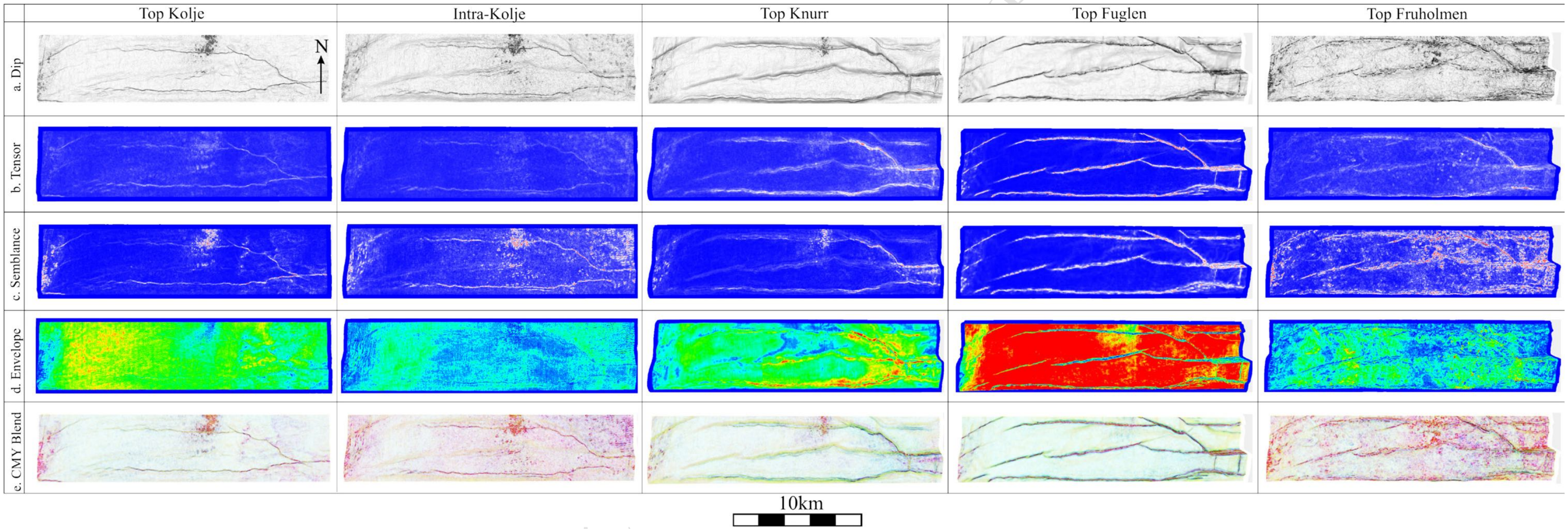

Top Kolje
Intra-Kolje
Top Knurr
Top Fuglen
Top Fruholmen
a. Dip
b. Tensor
c. Semblance
d. Envelope
e. CMY Blend
N
10km

Highlights:

- A fault analysis workflow was applied on seismic from the Snøhvit Field, Barents Sea
- E-W trending faults show highest dip distortion and throw in east of study area
- A fault enhancement filter was used to classify unsupervised seismic fault facies
- Seismic amplitudes present systematic brightening and dimming when nearing faults
- Fault facies correlate with throw, displacement gradient and mechanical stratigraphy